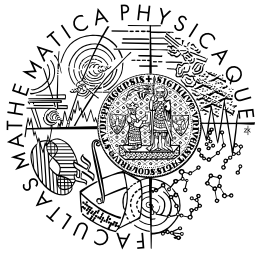

FACULTY
OF MATHEMATICS
AND PHYSICS
Charles University

**MASTER THESIS**

Anna Rosenkrancová

# Spectroscopic analysis of carotenoids in living organisms

Institute of Physics

Supervisor of the master thesis: Doc. RNDr. Peter Mojzeš, CSc.
Consultant of the master thesis: RNDr. Ing. Jana Pilátová, Ph.D.
Study programme: Biophysics and Chemical Physics
Study branch: Experimental biophysics and chemical physics

Prague 2024

I declare that I carried out this master thesis independently, and only with the cited sources, literature and other professional sources. It has not been used to obtain another or the same degree.

I understand that my work relates to the rights and obligations under the Act No. 121/2000 Sb., the Copyright Act, as amended, in particular the fact that the Charles University has the right to conclude a license agreement on the use of this work as a school work pursuant to Section 60 subsection 1 of the Copyright Act.

In ..... date .....  .....

Author's signature

I would like to thank my supervisor, Doc. RNDr. Peter Mojzeš, CSc., for his professional guidance, consultation, and interesting insights, especially into Raman microscopy. My thanks also go to my consultant, RNDr. Ing. Jana Pilátová, Ph.D., for introducing me to biology, always having new ideas, and encouraging me to try different experimental techniques. I also appreciate RNDr. Pavel Malý, Ph.D., who dedicated his time to measuring the FLIM and ixFLIM with me. Finally, I would like to thank Mgr. Tomáš Malina, who assisted with the HPLC work.

Title: Spectroscopic analysis of carotenoids in living organisms

Author: Anna Rosenkrancová

Institute: Institute of Physics

Supervisor: Doc. RNDr. Peter Mojzeš, CSc., Institute of Physics

Consultant: RNDr. Ing. Jana Pilátová, Ph.D., Lawrence Berkeley National Laboratory

Abstract: This thesis focuses on characterizing the spectroscopic properties of carotenoids, the most frequently occurring biomolecules in living organisms, using Raman and fluorescence microscopy techniques. The aim is to determine whether carotenoids are the source of the observed green autofluorescence (GAF) in various organisms. The study analyzed pure carotenoids, including β-carotene and astaxanthin, and *in vivo* samples from microorganisms such as *Haematococcus pluvialis*, *Vischeria* sp., and *Rhodotorula glutinis*. Fluorescence spectra of β-carotene and astaxanthin exhibited peaks in the green region, with β-carotene ranging from 524 nm to 545 nm and astaxanthin redshifted to 556 nm to 574 nm. Both carotenoids displayed bathochromic shifts in solvents with higher refractive indices. Under blue excitation, the chemical maps of carotenoids in microorganisms showed colocalization with the green fluorescence maps at around 530 nm, supporting the hypothesis that carotenoids contribute to GAF. Additionally, the green fluorescence maxima in *H. pluvialis* and *Vischeria* sp. align with the values measured in carotenoid standards, astaxanthin, and β-carotene, respectively. However, the study cannot exclude the potential presence of other fluorescent compounds, such as metabolites or degradation products, colocalizing with carotenoids. Therefore, while evidence suggests carotenoids as a source of GAF, further experiments are needed to confirm their role definitively.

Keywords: carotenoids, green autofluorescence, Raman microscopy, fluorescence microscopy, microorganisms, microalgae, cells, biological tissues

# Contents

# Introduction

Carotenoids are a fascinating class of pigments found naturally in a variety of photosynthetic bacteria, yeast, algae, fungi, plants, and animals. These compounds are responsible for the vibrant red, orange, and yellow colors seen in many fruits and vegetables, such as carrots, tomatoes, and bell peppers [Maoka, 2020, Bozalan and Karadeniz, 2011, Hassan et al., 2019]. Additionally, they contribute to the stunning autumn colors in leaves [Sanger, 1971]. In photosynthetic organisms, carotenoids play a crucial role in the process of photosynthesis by protecting chlorophyll from photodamage and aiding in light absorption [Hashimoto et al., 2016, Maoka, 2020].

Carotenoids are also renowned for their antioxidant properties, which help neutralize free radicals in the body, thereby reducing oxidative stress and lowering the risk of chronic diseases such as cardiovascular diseases and certain types of cancer. Notably, β-carotene, a type of carotenoid, is a precursor to vitamin A, which is essential for vision, immune function, and skin health [Stahl and Sies, 2012, 2003, 2007, Zia-Ul-Haq et al., 2021].

Despite extensive research into the chemical and photophysical properties of carotenoids and their involvement in various biological processes, many potential functions of these compounds remain unclear. For example, several studies have identified carotenoids as a potential source of green autofluorescence (GAF) in living systems [Kleinegris et al., 2010, Blankenhorn and Braunstein, 1958]. Autofluorescence is a widespread phenomenon observed across the entire spectrum of visible light [Lagorio et al., 2015]. For instance, blue autofluorescence of NAD(P)H is utilized to study energetic metabolism, while orange fluorescence of lipofuscin, found in the retinal pigment epithelium cells of the eye, is used to diagnose retinal diseases [Adler et al., 2015, Croce and Bottiroli, 2014, Călin et al., 2021]. Red fluorescence of chlorophyll is employed to assess the physiological condition of plants [Donaldson, 2020]. In summary, studying and characterizing autofluorescence is a powerful tool for diagnosis, monitoring the physiological state of biological substrates, observing inter-species communication, and indicating the presence of specific chemical compounds [Lagorio et al., 2015].

A wide range of species, including green algae, dinoflagellates, and various tissues, exhibit GAF under blue excitation. However, the molecular basis of GAF, in many instances, remains unknown [Ettema et al., 2022, Tang and Dobbs, 2007]. Carotenoids, which fluoresce in the green region and are among the most frequently occurring biomolecules in living systems, are a suitable candidate for the source of GAF [Gillbro and Cogdell, 1989, Maoka, 2020]. Some studies have already linked GAF to carotenoids. For example, GAF was observed in the orange lipid droplets of the green algae *Dunaliella salina* and in a pathological context in atherosclerotic plaques. In both cases, researchers claim that GAF originates from carotenoids [Kleinegris et al., 2010, Blankenhorn and Braunstein, 1958]. GAF has also been observed in amyloid-beta plaques in Alzheimer's disease, where the authors did not specifically attribute the fluorescence to carotenoids but observed a Raman signal of carotenoids in the plaques [Ettema et al., 2022].

On the other hand, the fluorescence of carotenoids is very weak, with quantum yields in order $10^{-4}$ [Bondarev and Knyukshto, 1994], raising uncertainties about

the feasibility of detecting green fluorescence of carotenoids in living systems. Lagorio et al. [2015] suggest that in flowers, the low fluorescence quantum yield of carotenoids, coupled with the overlap between carotenoid emission and the absorption spectra of other pigments in plants, likely prevents the observation of carotenoid emission.

The goal of this study is to further explore the potential of carotenoids to contribute to the autofluorescence of organisms in the green region by studying them as pure substances and also *in vivo* in organisms. As carotenoids exhibit one of the strongest Raman signals among biomolecules, Raman microscopy is an ideal experimental technique for this work. Moreover, the fluorescence of carotenoids falls into the same spectral region covered by multi-channel detection where the Raman signal of carotenoids in blue excitation is detected, which enables us to observe these two phenomena simultaneously [Gillbro and Cogdell, 1989, Llansola-Portoles et al., 2022].

This thesis provides an introduction to the experimental techniques, summarizes several studies exploring GAF, introduces the photophysics of carotenoids and their functions, discusses methods including sample preparation, equipment, measurement procedures, and data analysis, presents results from two common carotenoids (β-carotene and astaxanthin) and three living organisms (terrestrial yellow-green algae *Vischeria* sp., freshwater green algae *Haematococcus pluvialis*, and yeast *Rhodotorula glutinis*), includes in-depth discussions of these findings and ends with a detailed summary of the research.

# 1. Microscopic techniques

## 1.1 Fluorescence microscopy

### 1.1.1 Fluorescence

Luminescence is the emission of light not resulting from heat. It is a process in which energy absorbed by a substance is released in the form of light. There are various types of luminescence, including chemiluminescence, bioluminescence, triboluminescence, and photoluminescence, depending on the excitation mechanism. Fluorescence is a type of photoluminescence where the excited states are created by light [Olympus Web Resource on fluorescence].

A molecule absorbs photons at a specific wavelength (excitation) and then emits photons at a longer wavelength (emission). The mechanism can be explained by the Jablonski diagram (see Fig. 1.1 [Schweizer et al., 2021]), which is a graphical representation of the electronic states of a molecule (thick black lines) and the transitions between these states due to the absorption and emission of photons. $S_0$ is the ground electronic state of the molecule. $S_1$ $S_2$ are excited singlet states. Absorption (depicted in green) occurs almost instantaneously, on the order of $10^{-15}$ seconds. The excited molecules then rapidly relax through internal conversion and vibrational relaxation to the lowest vibrational level of $S_1$. Fluorescence (depicted in blue) subsequently occurs from the lowest vibrational level of the first excited singlet state ($S_1$) within $10^{-9}$ to $10^{-7}$ seconds, regardless of the excitation light's wavelength—this phenomenon is known as Kasha's Rule. Alternatively, relaxation to the ground state can occur through non-radiative processes (depicted in yellow) [Olympus Web Resource on fluorescence].

Besides direct relaxation from the S1 state to the ground $S_0$ state, intersystem crossing transitions can occur from an excited singlet state ($S_1$) to a triplet state ($T_1$). The emission of a photon as the molecule transitions from the triplet state ($T_1$) to the ground state ($S_0$) is called phosphorescence (depicted in red), which occurs on much longer timescales ($10^{-3}$ to 100 seconds) than fluorescence [Olympus Web Resource on fluorescence].

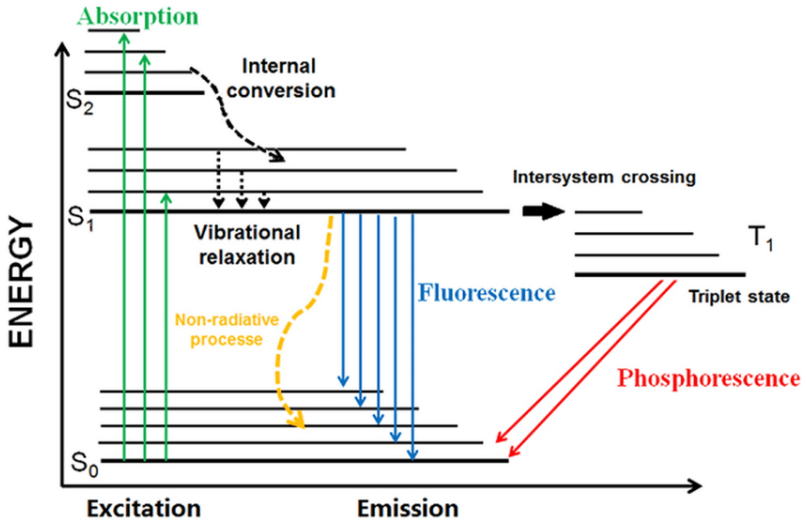


Figure 1.1: Jablonski Diagram illustrating the absorption, fluorescence, intersystem crossing, and phosphorescence processes. This diagram represents the electronic states of a molecule and the transitions between these states due to the absorption and emission of photons from Schweizer et al. [2021].

### 1.1.2 Widefield fluorescence microscopy

Widefield fluorescence microscopy is a conventional method where the entire specimen is illuminated uniformly with light, usually in the ultraviolet, blue, or green regions. Fluorophores within the specimen absorb this light and re-emit it at a longer wavelength. This emitted light is then collected to form an image [Olympus Web Resource on widefield microscopy]. A scheme of a widefield fluorescence microscope is in Fig. 1.2 [wid]. The light source provides the excitation light, often from a mercury or xenon arc lamp, with specific filters to select the appropriate excitation wavelength. A dichroic mirror reflects the excitation light towards the specimen while allowing the emitted light to pass through to the detector. The objective lens focuses the excitation on the specimen and also collects emitted light. The emission filter selects the specific wavelength of emitted light to reach the detector, blocking any remaining excitation light. A detector is usually a CCD camera that captures the fluorescent signal and converts it into an image [Olympus Web Resource on widefield microscopy]. The primary limitation of widefield fluorescence microscopy is its inability to reject out-of-focus light, resulting in blurred images for thick specimens. This limitation is addressed by confocal microscopy discussed in next section 1.1.3 [Olympus Web Resource on confocal microscopy].

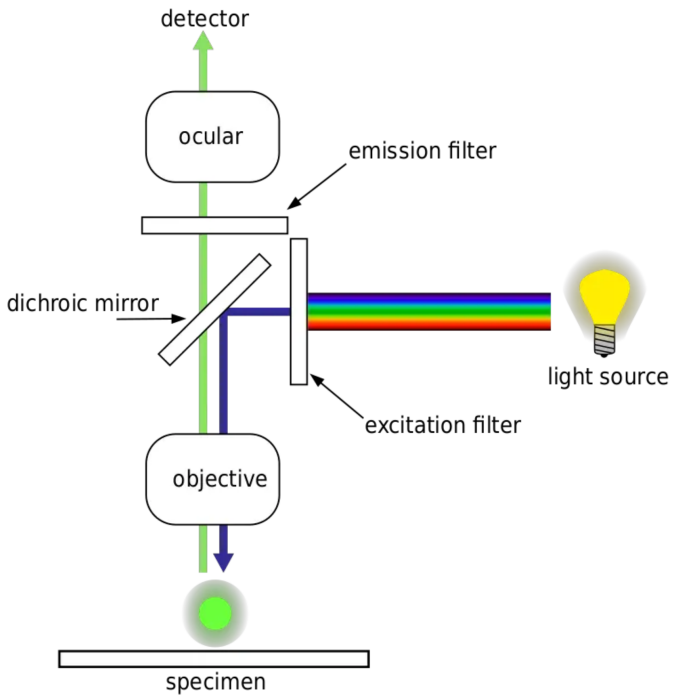


Figure 1.2: Working mechanism of fluorescence microscope from Microbe Online Web resource .

### 1.1.3 Confocal fluorescence microscopy

Confocal fluorescence microscopy enhances image resolution, especially in the Z-axis, and contrast by blocking out-of-focus light. The principle is illustrated in Fig. 1.3 from Abdi and Atighehchian [2022]. It is similar to widefield fluorescence microscopy with a few key differences. Instead of a lamp, the light source is a laser (Point Source in Fig. 1.3), providing a highly focused beam of light at specific wavelengths, allowing precise illumination of a single point in the specimen. In front of the detector, a pinhole aperture (Emission aperture in Fig. 1.3) is positioned. This aperture is conjugated to the focal plane of the objective lens, blocking out-of-focus light (depicted by yellow and orange lines in Fig. 1.3) and ensuring that only the fluorescence from the focal plane (depicted by blue lines in Fig. 1.3) reaches the detector. This spatial filtering significantly enhances image contrast and resolution [Olympus Web Resource on confocal microscopy].

Unlike widefield microscopy, where the image is collected all at once, confocal microscopy scans the specimen point by point. This requires a scanning system, typically consisting of oscillating mirrors or a moving stage, to move the laser beam across the specimen in a raster pattern. This enables point-by-point illumination and collection of fluorescence. By scanning the laser across the specimen, a high-resolution image of a thin optical section is obtained. Multiple optical sections can be combined to create a detailed three-dimensional reconstruction of the specimen [Olympus Web Resource on confocal microscopy].

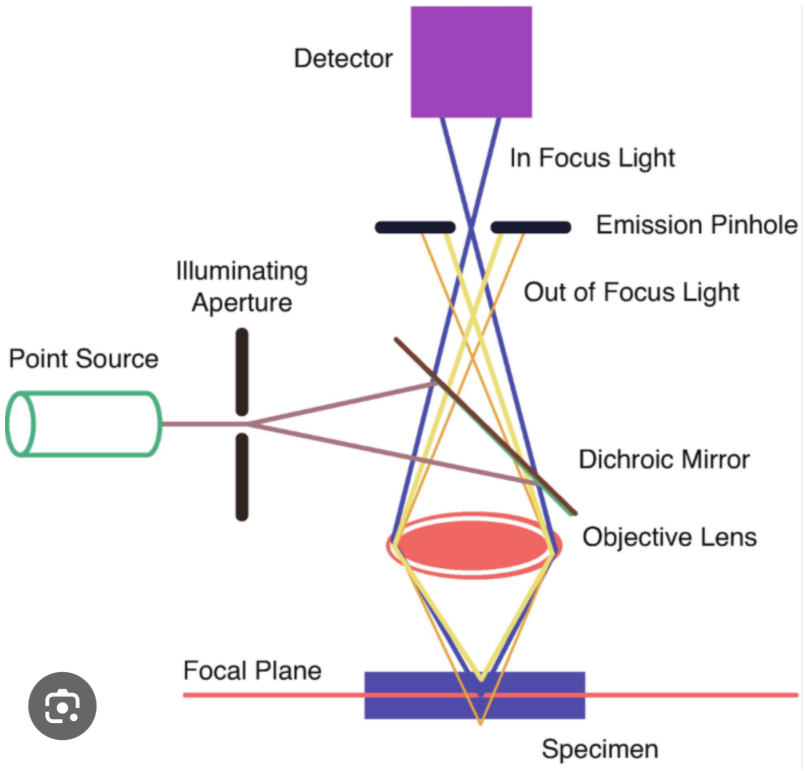


Figure 1.3: Schematic diagram of a confocal fluorescence microscope from Abdi and Atighehchian [2022].

## 1.2 Raman microscopy

### 1.2.1 Raman scattering

Raman scattering is a phenomenon where light interacts with the vibrational modes of molecules, resulting in a change in the energy of the scattered light. Discovered by Indian physicist C.V. Raman in 1928, this effect provides valuable insights into molecular vibrations, which are essential for understanding molecular structures and interactions [Raman and Krishnan, 1928].

When light encounters a molecule, most photons are elastically scattered, retaining their original energy in a process known as Rayleigh scattering. This is depicted in the central part of the schematic diagram 1.4 from [Edinburgh Instruments Raman Web resource], where the green arrow indicates that the energy of the scattered light remains the same as the incident light [Long, 2002].

However, a small fraction of photons are inelastically scattered, leading to a shift in their energy. This shift can be observed as either a Stokes or an anti-Stokes shift. As shown in the schematic 1.4, the Stokes shift (indicated by the red arrow) occurs when the scattered photon has lower energy than the incident photon, as the molecule gains energy and transitions to a higher vibrational state. Conversely, the anti-Stokes shift (depicted with a blue arrow) happens when the scattered photon has higher energy than the incident photon, typically because the molecule is initially in an excited vibrational state and loses energy upon scattering. The lower part of the schematic 1.4 illustrates the Raman shifts graphically: the Stokes shift results in a peak at a higher wavelength (lower

energy) compared to the incident light ($\lambda_0$), while the anti-Stokes shift results in a peak at a lower wavelength (higher energy) [Long, 2002].

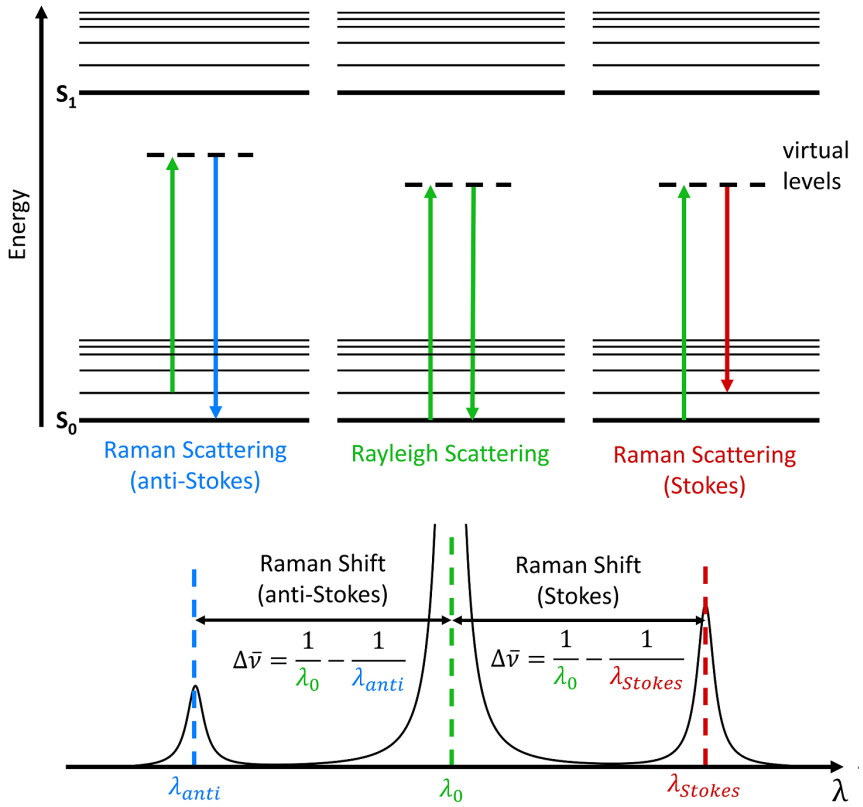


Figure 1.4: Schematic diagram illustrating Rayleigh scattering, Stokes shift, and anti-Stokes shift from Edinburgh Instruments Raman Web resource.

### Classical theory

In the classical theory, the polarization $P$ of a molecule in an electric field $E$ is given by:

$$P = \alpha E \tag{1.1}$$

where $\alpha$ is the polarizability of the molecule. For Raman scattering, the incident electric field $E$ can be represented as:

$$E = E_0 \cos(\omega_0 t) \tag{1.2}$$

where $E_0$ is the amplitude and $\omega_0$ is the frequency of the incident light. The polarizability $\alpha$ varies with the vibrational motion of the molecule:

$$\alpha = \alpha_0 + \left(\frac{\partial \alpha}{\partial Q}\right)_0 Q \tag{1.3}$$

where $Q$ is the vibrational coordinate. The vibrational coordinate $Q$ can be written as:

$$Q = Q_0 \cos(\omega_v t) \tag{1.4}$$

where $Q_0$ is the amplitude and $\omega_v$ is the vibrational frequency. Substituting $Q$ into the expression for $\alpha$ gives:

$$\alpha = \alpha_0 + \left(\frac{\partial \alpha}{\partial Q}\right)_0 Q_0 \cos(\omega_v t) \tag{1.5}$$

The induced dipole moment $P$ becomes:

$$P = \left(\alpha_0 + \left(\frac{\partial \alpha}{\partial Q}\right)_0 Q_0 \cos(\omega_v t)\right) E_0 \cos(\omega_0 t) \tag{1.6}$$

Using trigonometric identities, this can be expanded to:

$$P = \alpha_0 E_0 \cos(\omega_0 t) + \frac{1}{2}\left(\frac{\partial \alpha}{\partial Q}\right)_0 Q_0 E_0 \left[\cos((\omega_0 + \omega_v)t) + \cos((\omega_0 - \omega_v)t)\right] \tag{1.7}$$

The first term represents Rayleigh scattering, while the terms $\cos((\omega_0 + \omega_v)t)$ and $\cos((\omega_0 - \omega_v)t)$ represent the anti-Stokes and Stokes shifts, respectively.

Classically, the intensities of Stokes and anti-Stokes scattering should be similar. However, in reality, the intensity of anti-Stokes scattering is much lower. This discrepancy is due to the quantum mechanical nature of molecular vibrations and the Boltzmann distribution of energy states, which the classical theory does not consider. At thermal equilibrium, most molecules are in the ground vibrational state, making Stokes scattering more probable than anti-Stokes scattering, which requires molecules to be in excited vibrational states. Quantum mechanical calculations are necessary to accurately describe the Raman scattering process, as they take into account the discrete energy levels and the probabilistic nature of molecular vibrations [Long, 2002].

### Resonance Raman

Standard Raman scattering is an inherently weak process, with only about one in $10^6$ to $10^8$ photons undergoing Raman scattering. This low efficiency can make it difficult to detect Raman signals without sensitive equipment. One way to enhance the intensity is by resonance. Resonance Raman scattering occurs when the incident light frequency is close to the electronic transition frequency of the molecule. This resonance condition can enhance the Raman scattering intensity by several orders of magnitude, sometimes by factors of $10^3$ to $10^6$. This significant enhancement occurs because the polarizability tensor becomes much more responsive to the incident light frequency, increasing the probability of inelastic scattering [Long, 2002].

### 1.2.2 Confocal Raman microscopy

Confocal Raman microscopy combines the principles of confocal microscopy with Raman spectroscopy to provide detailed chemical information with high spatial resolution. This technique is non-destructive, making it suitable for studying sensitive and valuable samples without causing damage [Dieing et al., 2011].

As with confocal fluorescence microscopy, confocal Raman microscopy uses spatial filtering to eliminate out-of-focus light. The principle of confocality explained above 1.1.3 applies here as well. The confocal setup enables depth profiling, allowing for the acquisition of Raman spectra at different depths within the sample, providing three-dimensional chemical maps [Dieing et al., 2011].

The scheme of the Raman microscope is in Fig. 1.5. The laser source provides the excitation light, typically a monochromatic laser with a specific wavelength suitable for Raman excitation. The beam splitter directs the laser beam towards the sample while allowing the scattered light to pass through to the detector. The objective lens focuses the laser beam onto a small spot within the sample and collects the scattered light. A Rayleigh rejection filter blocks the elastically scattered Rayleigh light, allowing only the inelastically scattered Raman light to pass through. The confocal pinhole ensures that only light from the focal plane reaches the detector, blocking out-of-focus light. The collected Raman scattered light is then directed through the entrance slit of a spectrograph, where diffraction gratings disperse the light into its component wavelengths. The CCD camera captures the Raman signal. Confocal Raman microscopy scans the specimen point by point. This requires a scanning system, typically involving a moving sample stage, to move the laser beam across the specimen in a raster pattern. At each point, a Raman spectrum is collected, enabling the construction of a high-resolution image of the sample [Dieing et al., 2011].

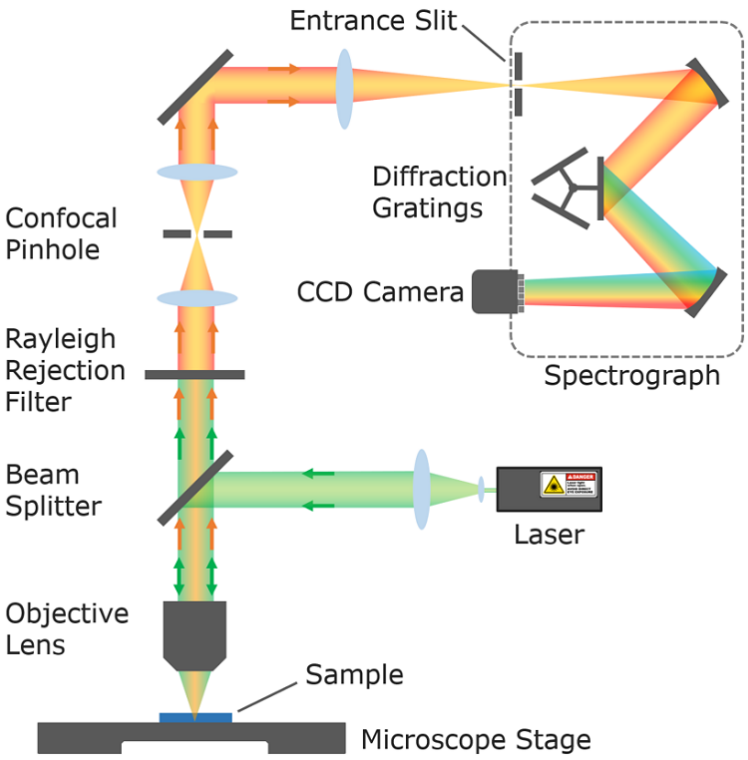


Figure 1.5: Schematic diagram of a confocal Raman microscope from Edinburgh Instruments microscope Web resource.

# 2. Green autofluorescence (GAF)

Fluorescence is emitted by a variety of living organisms, spanning from plants to insects and even humans [Lagorio et al., 2015, Ettema et al., 2022]. Investigating fluorescence properties and characteristics offers valuable insights into physiological conditions and inter-species communication and can signal the presence of specific chemical compounds [Lagorio et al., 2015]. A common phenomenon observed is green autofluorescence (GAF) under blue excitation [Tang and Dobbs, 2007, Tsuji, 2010, Lagorio et al., 2015, Ettema et al., 2022]. While the origins of GAF are well understood in some cases, such as the green fluorescent protein (GFP) in bioluminescent hydromedusa *Aequorea victoria* or photoreceptive flavoprotein in the flagella of brown algal swarmers [Tsuji, 2010, Kawai, 1992], the molecular basis of GAF in many organisms remains unknown [Tang and Dobbs, 2007, Khandelwal and Saxena, 2007].

Tang and Dobbs [2007] observed GAF with excitation in blue or UV light in various microorganisms. Research across diverse microalgal taxa, including dinoflagellates, diatoms, green algae, cyanobacteria, and raphidophytes, has unveiled green autofluorescence as a common feature, particularly evident in cellular structures such as eyespots, accumulation bodies, spines, and aerotopes. While some instances of GAF were found near chloroplasts, they weren't always colocated with chlorophyll-related red autofluorescence within cells. GAF was also observed in cellular structures lacking chlorophyll, such as dinoflagellate eyespots, green algae spines, and cyanobacteria aerotopes. The widespread occurrence of GAF across various organisms suggests it may be caused by compounds commonly found in microalgal cells. However, the exact origin of GAF is not known.

Tang and Dobbs [2007] also pointed out that the observed GAF interferes with the emission of green-fluorescing stains, often used in research without any concern regarding GAF.

Several authors attributed GAF to carotenoids. Kleinegris et al. [2010] studied the green fluorescence in another green algae, Dunaliella salina, known for its capacity to produce carotenoids, which are primarily stored in lipid globules. Under stress conditions, D. salina cells begin to synthesize carotenoids, transitioning from a green to an orange appearance as the chloroplast shrinks and carotenoid-containing lipid globules form. Fluorescence microscopy revealed a noticeable change in fluorescence patterns after stress. The red fluorescence from chlorophyll decreased, while green fluorescence emerged.

To confirm that carotenoids are responsible for the green fluorescence, researchers isolated the carotenoid-rich globules. After isolating these globules, they used confocal laser scanning microscopy (CLSM) to detect the fluorescence. The isolated globules showed a clear orange color under light microscopy, and upon CLSM examination, they emitted green fluorescence. This finding verified that the fluorescence originated from the carotenoid-containing globules and not from other cellular components or the surrounding solution. The ratio between the quantum yields of β-carotene and chlorophyll supported this conclusion [Kleinegris et al., 2010].

Another study attributing GAF to carotenoids observed that it also appears in pathological contexts - in atherosclerotic plaques. Blankenhorn and Braun-

stein [1958] studied green fluorescence within plaques under UV light excitation. They identified different fluorescence types, correlating them with the severity of the lesions. In Grade II plaques, green fluorescence appears faint and sporadic, mainly visible in lipid-bearing areas. As the severity increases to Grade III and IV, the fluorescence becomes more intense and widespread, presenting as bright and dim patches of green fluorescence. Interestingly, these green fluorescent regions are often found in areas rich in lipids, and previous extractions have shown that carotenoids are present in these regions. This finding suggests that carotenoids may significantly contribute to the observed fluorescence in atherosclerotic plaques [Blankenhorn and Braunstein, 1958].

Very recently, a study focusing on fluorescence lifetime imaging (FLIM) of fluorescence in the yellow-green region, supposedly coming from carotenoids, was published. Solovchenko et al. [2024] utilized FLIM to investigate the fluorescence lifetimes of carotenoids in microalga *Bracteacoccus aggregatus* cells using 750 nm two-photon excitation. The FLIM data were manually clustered into three main groups based on lifetime values. Cluster #1, with the shortest lifetimes (approximately 200 ps in the green stage), was assigned to chloroplasts in intact cells, containing mostly primary carotenoids. Cluster #2, with moderately short lifetimes (approximately 250-1000 ps, depending on the growth stage), was associated with oleosomes, structures harboring secondary carotenoids. Cluster #3, with the longest lifetimes (up to 1400 ps), corresponded to degrading cells and spores. The shorter lifetimes were attributed to primary carotenoids present mostly in the green stage, while the longer ones were linked to secondary carotenoids observed in the later red stage.

Ettema et al. [2022] observed green autofluorescence in amyloid-beta plaques occurring in Alzheimer's disease. Apart from green autofluorescence, blue fluorescence is also observed. Specifically, blue autofluorescence appears when the sample is illuminated with UV light (340–380 nm), and green autofluorescence appears under blue light illumination (450–490 nm). This fluorescence is used to locate plaques, which are then confirmed through staining with thioflavin-S, a compound that binds to amyloid, making the plaques appear as yellow areas in the fluorescence images.

Raman microscopy further confirms the presence of carotenoids in the plaque areas, showing characteristic peaks around 1150 and 1514 $cm^{-1}$. Comparing these spectra with reference carotenoid spectra indicates a strong match, particularly with lycopene when adsorbed onto aggregated Aβ42 peptides [Ettema et al., 2022]. Although the authors do not specifically attribute the GAF to carotenoids, the colocalization is certainly intriguing.

Aging erythrocytes have been observed to exhibit an increase in GAF, as reported by a study that examined the fluorescence properties of blood erythrocytes across different age groups [Khandelwal and Saxena, 2007]. The study found that the intensity of green autofluorescence increased with the age of the erythrocytes.

The presence of carotenoids in erythrocytes has been documented in previous research. Mathews-Roth [1975] reported the presence of carotenoids in the erythrocyte membranes of both carotenemic and noncarotenemic individuals, indicating that these compounds are a regular component of erythrocyte membranes regardless of dietary intake. Further research has shown that β-carotene can induce alterations in hemoglobin affinity to oxygen. A study published in 2021

found that β-carotene affects the structural properties of hemoglobin, potentially influencing its function [Fiedor et al.]. This study provides additional evidence that carotenoids, including β-carotene, are present in erythrocytes. Even though Khandelwal and Saxena [2007] did not indicate the origin of GAF in erythrocytes, these finding supports the hypothesis that carotenoids could contribute to the observed GAF in aging erythrocytes.

# 3. Carotenoids

Carotenoids are tetraterpene pigments absorbing mostly in the blue region of the visible spectrum, which leads to their typical yellow, orange, and red color [Frank and Christensen, 2008, Maoka, 2020]. The color of some common carotenoids is shown in Fig 3.1. They are one of the most frequently occurring biomolecules in living organisms found in photosynthetic bacteria, certain archaea and fungi, algae, plants, and animals. Typically composed of eight isoprene units forming a 40-carbon skeleton, carotenoids generally feature a polyene chain with nine conjugated double bonds and end groups at both chain ends. Carotenoids are classified into two groups: carotenes and xanthophylls. Carotenes, such as α-carotene, β-carotene, and lycopene, are hydrocarbons, with approximately 50 types existing in nature. In contrast, xanthophylls like β-cryptoxanthin, lutein, zeaxanthin, astaxanthin, fucoxanthin, and peridinin contain oxygen atoms, presenting hydroxy, carbonyl, aldehyde, carboxylic, epoxide, and furan-oxide groups. As structures of xanthophylls are very diverse, about 800 varieties have been described in nature [Maoka, 2020]. Structures of some common carotenes and xanthophylls are depicted in Fig. 3.1 from Naz et al. [2023].

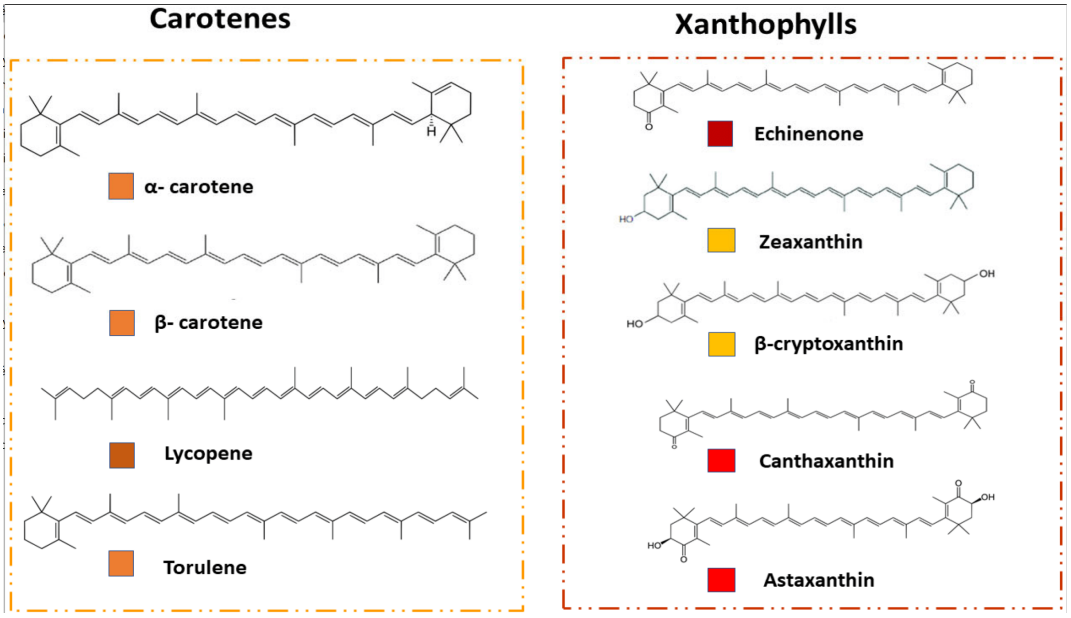


Figure 3.1: Chemical structure of a few common carotenes and xanthophylls, with the color of each compound indicated in squares below the structures from Naz et al. [2023].

## 3.1 Photochemistry of carotenoids

### 3.1.1 Carotenoids as linear polyenes

The characterization of carotenoids follows from the description of simple all-trans-polyenes. According to symmetry theory, these polyenes belong to $C_{2h}$ point group. Symmetry labels for electronic states often used for carotenoids

are based on the symmetry operations of this group. For carotenoids, the low-energy singlet states, depicted in figure 3.2, are responsible for most of their specific photophysical properties [Frank et al., 2004]. The transition from the ground state $S_0$ ($1A_g^-$) to the first excited state $S_1$ ($2A_g^-$) is strongly forbidden, as it does not include change nor in the symmetry (u $\leftrightarrow$ g) and neither in the pseudoparity (+ $\leftrightarrow$ -). On the other hand, the transition to the second excited state $S_2$ ($1\,B_u^+$) is strongly allowed and responsible for the absorption in the mostly blue region of the visible spectrum [Frank and Christensen, 2008].

Most large organic molecules in condensed phases follow Kasha's rule and emit from the lowest singlet or triplet electronic state. Compared to them, the emission of carotenoids depends on the number of the conjugated double bonds. The emission ratio of $(S_2 \rightarrow S_0)$:$(S_1 \rightarrow S_0)$ increases with the number of conjugated double bonds. Carotenoids containing eight or fewer carbon-carbon double bonds display fluorescence bands associated with the $(S_1 \rightarrow S_0)$ transition. In longer carotenoids like β-carotene and lycopene, the fluorescence is weak and originates primarily from the $(S_2 \rightarrow S_0)$ transition, while the $(S_1 \rightarrow S_0)$ emission is negligible. The shift from $S_1$ to $S_2$ fluorescence is attributed to higher rates of $(S_1 \rightarrow S_0)$ non-radiative decay, driven by smaller $(S_1 - S_0)$ energy gaps and an increased density of $S_0$-accepting modes in longer conjugated systems. Consequently, the $(S_1 \rightarrow S_0)$ fluorescence diminishes, allowing the weaker residual $(S_2 \rightarrow S_0)$ emission to dominate in longer molecules [Frank and Christensen, 2008].

Another notable characteristic of the photochemistry of carotenoids is the absence of spin-forbidden phosphorescence from low-energy triplet states. The rate of phosphorescence seemingly cannot compete with fast non-radiative $(T_1 \rightarrow S_0)$ relaxation from low-energy triplet states [Frank and Christensen, 2008].

Gillbro and Cogdell [1989] reported fluorescence excitation and emission spectra of β-carotene, rhodopin and spheroidenone in carbon disulfide ($CS_2$) at room temperature. The fluorescence maxima for β-carotene appears in the green region around 560 nm, and its quantum yield is low ($6 \times 10^{-5}$). Bondarev and Knyukshto [1994] observed a bathochromic shift at the increase of the solvent´s refractive index in both $(S_2 \leftrightarrow S_0)$ fluorescence and absorption of β-carotene. The fluorescence maxima were 522 nm in *n*-hexane, 535 nm in toluene, and 565 nm in carbon disulfide at room temperature. The $S_2$ fluorescence quantum yields were $1.3 \times 10^{-4}$, $1.2 \times 10^{-4}$, $1.6 \times 10^{-4}$ respectively [Bondarev and Knyukshto, 1994].

Such low quantum yields cast doubt on whether the GAF in organisms originates from carotenoids, as other sources of fluorescence in organisms exhibit notably higher quantum yields, such as 0.79 for GFP and 0.25 for chlorophyll [Lagorio et al., 2015, Forster and Livingston, 1952]. However, the fluorescence of compounds with quantum yields in the same order as carotenoids has been observed. Red emission of anthocyanin, a member of the flavonoid family, was observed in the petals of *Rhododendron indicum* with quantum yields between $2.4 \times 10^{-5}$ and $1.9 \times 10^{-4}$ [Lagorio et al., 2015].

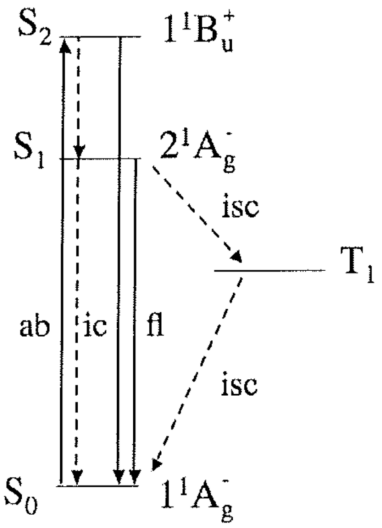


Figure 3.2: Electronic low-energy singlet states ant triplet state of all-trans-polyenes belonging to the $C_{2h}$ point group often used for carotenoids. ab = absorption; ic = internal conversion; fl = fluorescence; isc = intersystem crossing. From Frank et al. [2004].

### 3.1.2 Other singlet excited states of carotenoids

As described above, carotenoids are often simplified as linear polyene molecules, but this approach may overlook the impact of functional groups present in carotenoids. The description of simple polyenes assumes planarity, which the groups can perturb. What's more, carotenoids in light-harvesting complexes are notably distorted. The functional groups contribute significantly to the more complex behavior than initially predicted for simple linear polyenes and complicate the interpretation of carotenoid's singlet excited states [Hashimoto et al., 2018].

It was thought that as the $S_1 - S_2$ energy gap increases with a number of conjugated double bonds, the $S_2$ lifetime should also increase. However, experiments studying the relation between the number of conjugated double bonds and $S_2 \rightarrow S_1$ internal conversion rate did not find any dramatic effect on the $S_2$ lifetime. This led to a proposition of intermediate states and more complicated relaxation schemes depicted on 3.3 [Polívka and Sundström, 2004]. The presence of states $1^1B_u^-$ and $3^1A_g^-$ was predicted already in theoretical calculations of linear polyenes. The $S^*$ state was discovered in free carotenoids in solutions and in carotenoids bound to light-harvesting complexes. Interestingly, this state decays into a triplet state in the bound form, but the carotenoid in solution does not form the triplet state. The understanding of $S^*$ state may not be accurate within the $C_{2h}$ framework.

Carotenoids containing carbonyl groups can form intramolecular charge-transfer states $S_{ICT}$ responsible for the carotenoid to chlorophyll charge transfer high efficiency. This process has been well-documented in carotenoids like peridinin and fucoxanthin [Hashimoto et al., 2018]. Additionally, the existence of $S_{ICT}$ states in carotenoids demonstrates the significant role that specific functional groups can play in altering the electronic properties of these molecules.

Many other forbidden excited singlet states have been reported. Still, quite

often, there is an unclear interpretation of the data, as the presence of these states complicates the spectral analysis and the understanding of the relaxation pathways. As noted by Hashimoto et al. [2018], the diversity of possible excited states and their interactions necessitates a more detailed theoretical and experimental framework to comprehend the behavior of carotenoids in various environments fully.

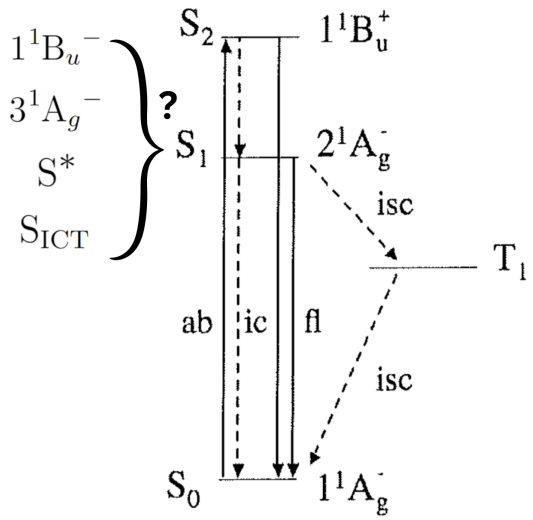


Figure 3.3: Energy level diagram depicting the notation of various additional singlet states under investigation. Adapted from Frank et al. [2004].

## 3.2 Raman spectra of carotenoids

Carotenoid molecules are highly suitable for resonance Raman studies due to their extremely high resonance enhancement, which is the highest among natural biomolecules [Llansola-Portoles et al., 2022]. Despite the diverse chemical structures within the broad family of carotenoid molecules, their resonance Raman spectra are remarkably similar. Because of the linear structure of carotenoids, their Raman spectra feature only a few intense bands. Remarkably, these bands are largely unaffected by the molecular environment. For example, the resonance Raman spectra of carotenoids dissolved in hexane are almost identical to those of protein-bound carotenoids [Robert, 1999].

The Raman spectra of carotenoids display several characteristic bands, each associated with different vibrational modes of the polyene chain. The most intense contribution, termed the $\nu_1$ band, appears around 1520 $cm^{-1}$ and arises from the stretching vibrations of the conjugated C=C double bonds, indicated in green color in Fig 3.4. The frequency of the $\nu_1$ band depends on the length of the $\pi$-electron conjugated chain and is sensitive to the molecular configuration of the carotenoid. As many of the relevant carotenoids consist of the 9 C=C polyene backbone, it is challenging to differentiate between various carotenoid compounds using Raman spectroscopy alone [Udensi et al., 2022, Llansola-Portoles et al., 2022].

Around 1160 $cm^{-1}$, the $\nu_2$ band can be observed (Fig 3.4 blue), which is a complex cluster of bands resulting from the combination of C-C stretching vibra-

tions and in-plane C-H bending modes. The $\nu_3$ band (Fig 3.4 pink), located at approximately 1000 $cm^{-1}$, is associated with in-plane rocking vibrations of the methyl groups attached to the conjugated chain, coupled with in-plane bending modes of adjacent C-H groups [Udensi et al., 2022, Llansola-Portoles et al., 2022]. These bands show high similarity across all carotenoids, indicating that the spectra are not very sensitive to the groups located at each end of the polyene chain, even though these groups typically determine the chemical structure [Robert, 1999].

Additionally, the $\nu_4$ band appears around 950-960 $cm^{-1}$ and arises from C-H out-of-plane wagging motions coupled with C=C torsional modes. These out-of-plane modes are typically weak unless there are distortions in the planar modes of the carotenoids, such as those caused by steric hindrance within a protein binding pocket [Udensi et al., 2022, Llansola-Portoles et al., 2022].

Further, weaker features, which are not resonantly enhanced, are mainly found between 1000 and 1400 $cm^{-1}$ and are attributed to C-H in-plane bending modes. Additional weak features at higher wavenumbers (e.g., 2169 $cm^{-1}$, 2526 $cm^{-1}$, 2679 $cm^{-1}$, and 2920 $cm^{-1}$) correspond to overtone and combination bands that arise from the total symmetric character of the carotenoid vibrations ($\nu_1$, $\nu_2$, and $\nu_3$) [Udensi et al., 2022].

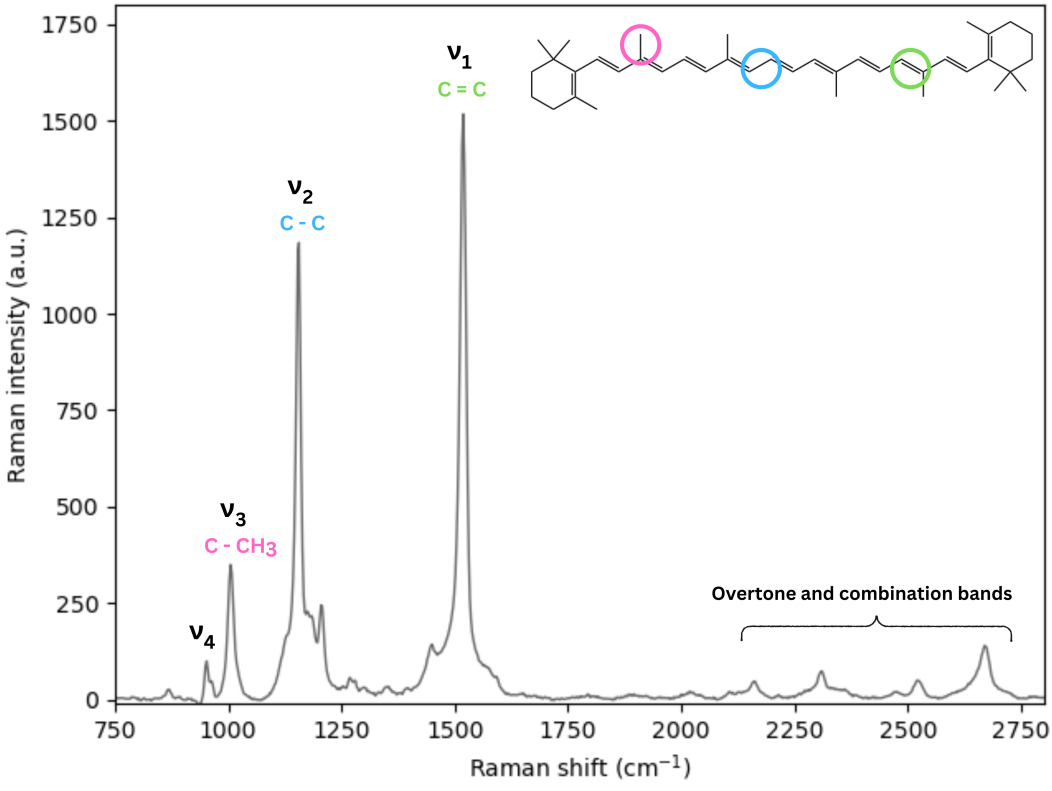


Figure 3.4: Raman spectrum of carotenoid from carrot root and structural formula of β-carotene. The function groups responsible for the certain Raman peaks indicated in the formula with colors: C–$CH_3$ (pink), C–C (blue), and C=C (green). Assignments of Raman peaks were performed according to Nikelshparg et al. [2022].

## 3.3 Function of carotenoids

Being one of nature's most widely distributed pigments, carotenoids exhibit a wide range of functions.

### 3.3.1 Carotenoids in photosynthesis

Carotenoids possess several roles in the process of photosynthesis. Firstly, they act as accessory light-harvesting pigments absorbing light in the blue-green region of the solar spectrum and subsequently transferring the captured energy to bacteriochlorophylls and chlorophylls [Hashimoto et al., 2016]. The energy scheme of this process is in 3.5 [Li et al., 2016]. The energy of both $S_1$ and $S_2$ levels can be transferred to neighboring chlorophyll, which gets to a singlet excited state. This phenomenon is called singlet-singlet energy transfer, and its overall efficiency varies from organism to organism [Swapnil et al., 2021]. Absorption of carotenoids broadens the spectral range over which light can support photosynthesis and thus enhances the efficiency of photosynthetic light reactions. While this mechanism does not contribute much to the overall light-harvesting capacity of plants, it is essential for organisms living in more challenging conditions (e.g., purple photosynthetic bacteria) [Hashimoto et al., 2016].

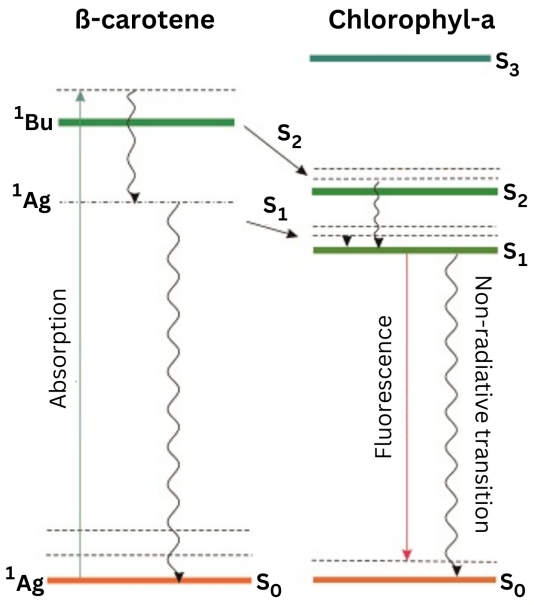


Figure 3.5: Energy scheme of β-carotene acting as an accessory light-harvesting pigment, absorbing light in the blue-green region of the solar spectrum and transferring the captured energy to (bacterio-)chlorophyll. The energy transfer involves both $S_1$ and $S_2$ levels, leading to a singlet excited state of chlorophyll, a process known as singlet-singlet energy transfer. Adapted from Li et al. [2016].

Secondly, carotenoids are essential for photosynthesis because of their ability to prevent photodamage. High light intensity leads to the formation of a chlorophyll triplet state, which may cause several unwanted reactions, e.g., photosensitization of singlet oxygen (red arrow in Fig. 3.6 [Hartzler et al., 2014]), one of the most aggressive oxidation agents. As shown in 3.6 (blue and green arrow),

carotenoids quench effectively both triplet chlorophyll and singlet oxygen. They absorb excessive energy from chlorophylls through triplet–triplet transfer and release excessive energy by polyene vibration. The mechanism of quenching oxygen is slightly different. Carotenoids take up thermal energy from singlet oxygen and release this energy by polyene vibration [Maoka, 2020].

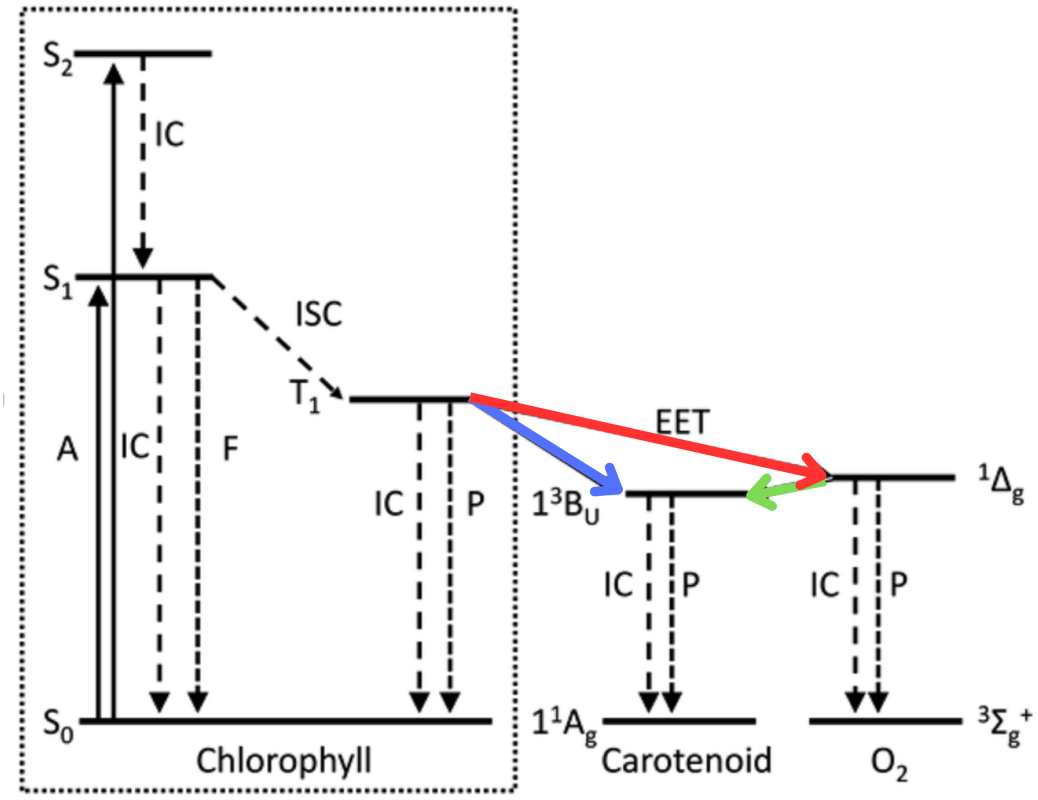


Figure 3.6: Simplified Chlorophyl energy level diagram showing the formation of the Chlorophyl triplet state ($T_1$ ) from the excited singlet state ($S_1$) followed by electronic energy transfer (EET) from the (B)Chl triplet state to a carotenoid molecule or an oxygen molecule. A = absorption, F = fluorescence, P = phosphorescence, IC = internal conversion, ISC = intersystem crossing. Adapted from Hartzler et al. [2014].

Another photoprotective mechanism is the Xanthophyll cycle. The process is explained in Fig. 3.7. In higher plants, xanthophyll cycles consist of violaxanthin–antheraxanthin–zeaxanthin. During light stress, violaxanthin is converted to zeaxanthin by the enzyme violaxanthin de-epoxidase (VDE in Fig. 3.7), while the reverse reaction is performed by zeaxanthin epoxidase ZE in Fig. 3.7). This cycle plays a key role in stimulating energy dissipation within light-harvesting antenna proteins and thus prevents photoinhibition [Maoka, 2020].

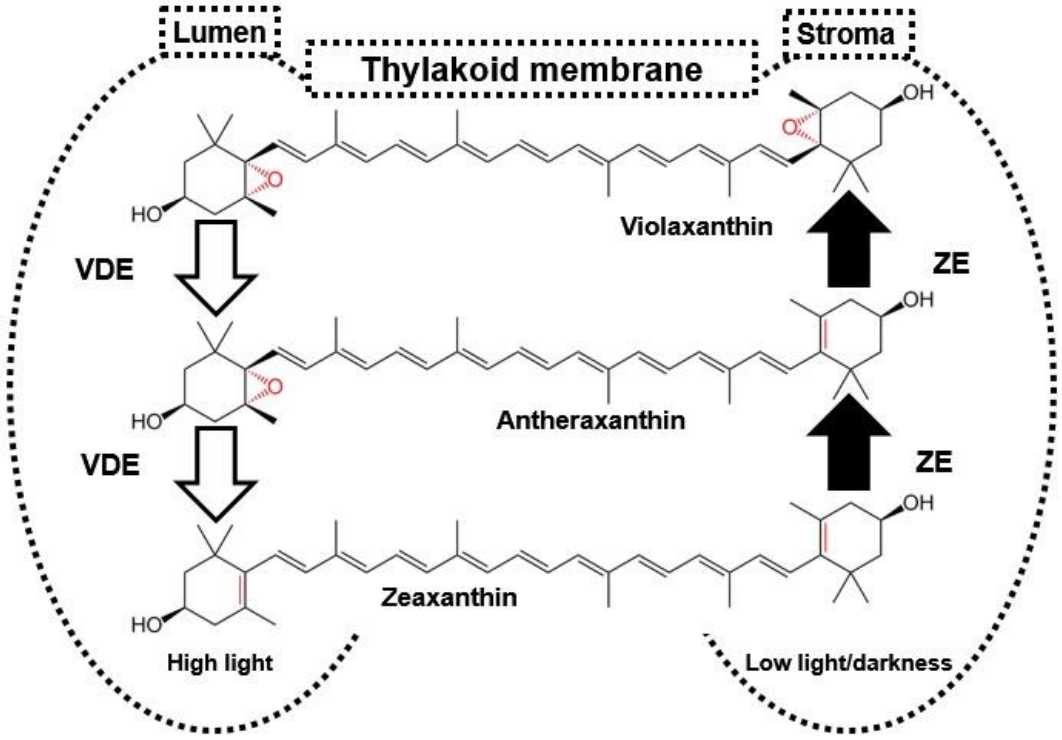


Figure 3.7: Reactions of the xanthophyll cycle in higher plants. VDE = violaxanthin de-epoxidase, ZE = zeaxanthin epoxidase. From Trojak and Skowron [2017].

Carotenoids occur not only in photosynthetic organs of plants but also in fruit, roots, seeds, and flowers. The vibrant color of carotenoids attracts insects and helps to pollinate plant species. A lot of fruits change color during ripening. A tomato is a good example when its exocarp turns from green to deep red. This transition happens due to chlorophyll degradation and the formation of red lycopene from colorless phytoene [Maoka, 2020, Campos et al., 2023, Zia-Ul-Haq et al., 2021].

### 3.3.2 Carotenoids as antioxidants

Carotenoids are also important antioxidants. Organisms with aerobic metabolism are exposed to the generation of reactive oxygen species (ROS). This species may cause DNA damage, protein oxidation, and lipid peroxidation. Carotenes, e.g., β-carotene, lycopene, and xanthophylls such as zeaxanthin and lutein quench singlet oxygen or free radicals in lipid phases and inhibit radical propagation chain during lipid peroxidation [Stahl and Sies, 2003]. For example, in human erythrocytes, carotenoids have been shown to inhibit lipid peroxidation and hemoglobin oxidation induced by ROS [Chisté et al., 2014].

Carotenoids are also particularly effective in protecting cell membranes from oxidative damage. The incorporation of carotenoids into the membrane structure enhances its resilience against environmental stressors Miki [1991]. What's more, carotenoids help maintain the function and integrity of biological membranes. They integrate into lipid bilayers and contribute to membrane fluidity and stability. The solubility of carotenoids is typically low in aqueous environments, except for xanthophylls that contain polar groups. Consequently, the distribu-

tion of carotenoids within biological membranes varies according to their specific types [Maoka, 2020, Zia-Ul-Haq et al., 2021].

The antioxidant activity of carotenoids can prevent the development of diverse diseases such as cancer, diabetes, and blindness [Zia-Ul-Haq et al., 2021].

# 4. Carotenoid content in model organisms

The objective of this work is to investigate the possible connection between GAF observed in various microorganisms and the carotenoids present in their organelles. To achieve this, we selected three model organisms known for their carotenoid production. These include two primary producers capable of synthesizing carotenoids— the algae *Haematococcus pluvialis* and *Vischeria* sp.— and one heterotrophic organism, the carotenoid-synthesizing yeast *Rhodotorula glutinis*. The following paragraphs provide basic information about these model organisms and their carotenoid content.

## 4.1 *Vischeria* sp. BOF79

*Vischeria* sp., classified under Stramenopiles - Eustigmatophyceae, is a genus of terrestrial yellow-green algae commonly found in soil crusts and on surfaces of rocks in various terrestrial habitats [Eliáš et al., 2017]. These algae are of significant interest due to their potential applications in biotechnology, thanks to their high lipid and carotenoid content [She et al., 2022, Stoyneva-Gärtner et al., 2019]. The study of Stoyneva-Gärtner et al. [2019] investigates the carotenoid content of five *Vischeria/Eustigmatos* strains from aero-terrestrial habitats in Bulgaria. The carotenoid content is summarized in Tab. 4.1. The content varied significantly across the strains; thus, the table presents the detected ranges. The carotenoids with the highest percentage are violaxanthin, lutein, and β-carotene.

Table 4.1: Carotenoid content of *Vischeria/Eustigmatos* strains reported by Stoyneva-Gärtner et al. [2019]. nd = not detected.

| Carotenoid | relative percentage |
|---|---|
| Vaucheriaxanthin | 3-8% |
| Violaxanthin | nd-32% |
| Luteoxanthin | nd-15% |
| Astaxanthin | 5-13% |
| Antheraxanthin | 12-19% |
| Lutein | 13-25% |
| Zeaxanthin | 8-11% |
| Canthaxanthin | nd-7% |
| β-carotene | nd-29% |

## 4.2 *Rhodotorula glutinis*

Rhodotorula, classified under Opisthokonta - Basidiomycota - Microbotryomycetes, is a genus of imperfect yeasts that includes species relevant to food spoilage

and medical contexts due to their allergenic potential. They exhibit an exclusively oxidative energy metabolism pathway and are unable to ferment. Rhodotorula is found in diverse habitats ranging from soil and freshwater to clinical specimens and marine environments, with occasional associations with mosquitoes and leaf-cutting ants. The colonies are often reddish, orange, or yellow as a result of the synthesis of carotenoid pigments [Yeeh, 1999].

The carotenoid composition of eighteen yeast species, including *Rhodotorula, Rhodosporidium, Sporobolomyces*, and *Sporidiobolus*, was analyzed by Buzzini et al. [2007]. The values for Rhodotorula glutinis, the species used in this work, are reported in Tab 4.2. The most abundant carotenoid is torularhodin, followed by torulene and β-carotene. A slight amount of γ-carotene is also present.

Table 4.2: Carotenoid content of *Rhodotorula glutinis* reported by Buzzini et al. [2007].

| Carotenoid | μg/g cell dry mass | relative percentage |
|---|---|---|
| Torularhodin | 52.5 | 46.8 % |
| Torulene | 34.3 | 30.6 % |
| γ-carotene | 5.1 | 4.5 % |
| β-carotene | 20.3 | 18.1 % |
| Total carotenoids | 112,2 | |

## 4.3 *Haematococcus pluvialis*

*Haematococcus pluvialis*, classified under Archaeplastida - Chlorophyta - Chlorophyceae, is a freshwater unicellular green microalga widely found across various habitats, ranging from brackish water to rock surfaces. It can survive harsh conditions, such as extreme temperatures and high salt concentrations, by forming protective cysts [Niizawa et al., 2021].

Its life cycle involves four distinct stages: macrozooids, microzooids, palmella, and haematocysts (aplanospores). In the early vegetative growth phase, the algae are in the macrozooid stage, characterized by spherical or ellipsoidal shape, biflagellates, and green color. In later stages, macrozooids transition into nonmotile palmella, eventually transforming into aplanospores. Aplanospores are resistant to extremely harsh conditions. Aplanospores are notable for their red coloration due to the accumulation of astaxanthin within lipid droplets in the cell. This makes *Haematococcus* one of the potent biological sources for astaxanthin production [Niizawa et al., 2021]. Astaxanthin forms up to 2-3 % of the cell on a dry weight basis [Ranga et al., 2009]. Ranga et al. [2009] identify the carotenoids from the *Haematococcus* cyst cell. The relative percentages of total carotenoid content from their study are in Tab. 4.3—the vast majority of carotenoid content in *H. pluvialis* is composed by astaxanthin esters.

Table 4.3: Carotenoid content of *Haematococcus pluvialis* reported by Ranga et al. [2009].

| Carotenoid | relative percentage |
|---|---|
| Astaxanthin esters | 83,70% |
| Free astaxanthin | 4,50% |
| Lutein | 3,80% |
| Zeaxanthin | 2,10% |
| β-carotene | 3,40% |
| $\alpha$-carotene | 1,70% |
| Violaxanthin | 1,50% |

# 5. Experimental

## 5.1 Materials

As suitable model compounds for this study, we selected the following carotenoids: one primary carotenoid taking part in photosynthesis - β-carotene and one secondary carotenoid not involved in photosynthesis - astaxanthin (USP reference standard, 1044200). Two different purities of β-carotene were used, namely 93% (Sigma-Aldrich, Product No. C9750) and 95% (Merck, synthetic, $\geq$ 95% (HPLC), Product No. C4582). Used solvents are summarised in Tab. 5.1.

The selection of model carotenoids for the present study was limited by their commercial availability. We are aware that, from the point of view of the carotenoids contained in the studied microorganisms (as shown in Tables 4.1, 4.2, and 4.3), it would be worthwhile to study the properties of a wider range of carotenoids, but it was beyond the time and financial possibilities of this thesis.

Table 5.1: Specifications of used solvents.

| Solvent | Purity | Label | Product number |
|---|---|---|---|
| Acetic acid | 99% *p.a.* | Penta | 200-580-7 |
| Acetone | for UV | Penta | 606-001-00-8 |
| Chloroform | *p.a.* | Lachema | 686 291 |
| Ethanol | 96% for UV | Penta | 603-002-00-5 |
| Hexane | 95% | Lachema | 40107 |
| Mineral oil | Ultra for molecular biology | Fluka | 69794 |
| Tetrahydrofuran | *p.a.* | Lachema | 308 860 702 |

## 5.2 Origin and cultivation of microorganisms

The origin and specification of the organisms are in Tab. 5.2.

*Haematococcus pluvialis* and *Vischeria* sp. were cultivated in Bold's Basal Medium, specifically designed for freshwater algae [Bischoff and Bold, 1963]. The cultivation occurred at room temperature, approximately 20 °C, under natural daylight provided by a north-facing window in the laboratory..

*R. glutinis* was cultivated on plates with yeast-peptobe-dextran medium at room temperature [YPD medium].

Table 5.2: Origin and classification of microorganisms.

| Species | Taxonomic classification | Origin | Code |
|---|---|---|---|
| *Vischeria* sp. BOF79 | Stramenopiles Eustigmatophyceae | CAUP - Culture Collection of Algae of Charles University, Prague, Czech Republic | Q202 |
| *Rhodotorula glutinis* | Opisthokonta Basidiomycota Microbotryomycetes | CCY - Culture Collection of Yeasts | 20-2-24 |
| *Haematococcus pluvialis* | Archaeplastida Chlorophyta Chlorophycea | CAUP - Culture Collection of Algae of Charles University, Prague, Czech Republic | G1002 |

## 5.3 Preparing samples of organisms

For microscopy measurements, around 10 µl of the cell suspension of *Haematococcus pluvialis* or *Vischeria* sp. was placed on a quartz slide, followed by the addition of approximately 5 µl of low melting agarose. This mixture was gently combined directly on the slide using a pipette. The preparation was then covered with a quartz coverslip, and any excess solution was carefully removed with a paper towel. The coverslip was sealed with the special fixing lacquer, CoverGrip Coverslip Sealant. The low melting agarose immobilizes the cells, preventing movement during measurement, while the CoverGrip sealant prevents sample evaporation.

To prepare the sample of *Rhodotorula glutinis*, a small portion of the culture was scooped from the plate and dissolved in distilled water; the subsequent procedure mirrored that of the algae preparation.

## 5.4 Absorption spectra

The absorption spectra of carotenoids in different solvents were measured using a Specord 250 dual-beam UV-visible absorption spectrometer from Analytik Jena equipped with a halogen lamp and a deuterium discharge lamp. Quartz absorption cuvettes (optical path 1 mm) were used for this measurement.

## 5.5 Fluorescence and Raman spectra of standards of carotenoid

The spectral characteristics of β-carotene and astaxanthin in various solvents were obtained using a confocal Raman microscope WITec alpha300 RSA, equipped with a 50× objective Zeiss EC Epiplan-Neofluar 50x/0.55 LD DIC (Zeiss, Germany). An extended working distance (FWD=9.1 mm) and a relatively high numerical aperture of 0.55 enabled the direct measurement of Raman spectra of carotenoids dissolved even in volatile solvents in hermetically sealed spectroscopic

cuvettes using the same Raman microscope as for biological samples (discussed later in section 5.7). Quartz absorption cuvettes (optical path 1 mm) were used for the measurement. The laser beam was focused on the reflection of the inner wall (glass-solution interface) and then shifted 50 μm into the solution. This approach ensures that the focus is equally deep in each sample. An excitation wavelength of 442 nm and power of 3.6 mW were employed. The data presented in the graphs are the average of three spectra acquired with an integration time of 2 seconds and 20 accumulations using the spectral stitching method.

## 5.6 Procesing of fluorescence and Raman spectra of carotenoid standards

The processing of the spectra was done using WITec Project 6.0 software. Cosmic spikes were removed, and the spectra of pure solvents were demixed.

For extracting the fluorescence position and intensity, a constant background was subtracted. Then, the spectra were fitted in Python using either single Gauss function:

$$f(x) = A\frac{1}{\sigma\sqrt{2\pi}}e^{-\frac{1}{2}\left(\frac{x-x_0}{\sigma}\right)^2} + H, \tag{5.1}$$

or sum of two Gauss functions:

$$f(x) = A_1\frac{1}{\sigma_1\sqrt{2\pi}}e^{-\frac{1}{2}\left(\frac{x-x_{01}}{\sigma 1}\right)^2} + A_2\frac{1}{\sigma_2\sqrt{2\pi}}e^{-\frac{1}{2}\left(\frac{x-x_{02}}{\sigma 2}\right)^2} + H. \tag{5.2}$$

To get the Raman band intensities without fluorescence background, it was subtracted using shape background subtraction.

## 5.7 Spectral maps and spectra of organisms

2D spectral maps of microorganisms were obtained using the same confocal Raman microscope, WITec alpha300 RSA (WITec, Germany), used for carotenoid solution measurements. The microscope was equipped with a water-immersion objective, UPlanSApo 60×, NA 1.20 (Olympus, Japan). Two excitation wavelengths were used: green (532 nm) and blue (442 nm).

The choice of the excitation wavelengths was determined by the availability of lasers at the Raman microscope used here (442, 532, 633, 647, 785, and 830 nm) and their suitability for the aims of this work. Lu et al. [2018] investigated the influence of excitation wavelength on Raman spectra of β-carotene in acetone. They found that 532 nm is optimal for Raman spectroscopy in biological tissues. This wavelength balances adequate resonance Raman enhancement and minimal fluorescence and self-absorption interference because it falls on the tail-end of the β-carotene absorption curve (see Fig. 5.1). Although the blue excitation (488 nm) showed the highest resonance Raman enhancement, it also had the highest fluorescence and self-absorption.

Since in this work we dealt with the connection between Raman scattering and GAF during excitation in the blue region, we used a He-Cd laser with emission at 442 nm for excitation. This excitation wavelength, together with a larger range of the detected spectral region, allowed the simultaneous registration of

Raman scattering and GAF. Additionally, this wavelength is near the absorption maximum of β-carotene (see Fig. 5.1), theoretically allowing us to observe fluorescence from carotenoids. However, the high fluorescence background and strong resonance Raman enhancement can obscure the Raman signals of other compounds. To address this issue, the 532 nm excitation wavelength becomes advantageous.

For the green excitation, we used two different laser powers. When exiting the Raman scattering of photosynthetic microorganisms with a relatively low power (only μW units), which does not cause significant photodamage (photobleaching), it is possible to simultaneously detect the Raman signal of carotenoids and the fluorescence signal of chlorophyll (emission maximum at 684 nm [Lamb et al., 2018]), or the fluorescence of other fluorophores present in the cell (e.g. yellow fluorescence with a broad band centered at ca 595 nm). The prerequisite for such simultaneous measurement of Raman and fluorescence signals is that the emissions of both fluorophores fall (at least partly) into the same spectral region covered by multi-channel detection where the Raman signal of carotenoids is detected. In the case of 532 nm excitation and using a spectrograph with a grating covering a wider spectral area (covering approximately a 3600 $cm^{-1}$ wide region), it was possible to simultaneously detect the Raman signal of carotenoids together with fluorescence in the yellow and red regions. In the red region, where the fluorescence of chlorophyll (max. 684 nm [Lamb et al., 2018]) is present, only the onset of the chlorophyll fluorescence band could be captured, but even this onset is sufficient for the construction of reliable fluorescence maps, which could be correlated with Raman maps of carotenoids and fluorescence maps of unspecified fluorophores emitting in yellow areas of the spectrum.

The advantage of this procedure is that information on the Raman signal of carotenoids, the fluorescence of chlorophyll, and the fluorescence of other fluorophores present in the cell can be obtained simultaneously from the same measurement. However, when measuring at low power, it is only possible to detect Raman scattering from molecules exhibiting resonance enhancement for a given excitation or, alternatively, have an exceptionally large effective Raman cross-section, as it is in the case of carotenoids or other linear molecules with conjugated bonds (polyenes). Other present molecules (e.g., lipids, starch, proteins, crystalline guanine) do not provide any detectable Raman scattering at such low excitation powers. Moreover, detection of their Raman spectra is often hindered by high fluorescence background from chlorophyll and other chromophores. To measure the Raman signal of these substances, it is necessary to use higher excitation intensities, and often to photobleach chlorophylls before measurement. The procedure mentioned above of successive measurements with low and high excitation powers was used for the spectral detection of carotenoids and other biomolecules.

Fluorescence spectra of organisms were measured under blue excitation (442 nm) immediately following the mapping measurements using the spectral stitching method. These spectra were fitted using a sum of Gaussian functions as described in Eq. 5.2. In some cases, a sum of three Gaussian functions was used, analogous to Eq. 5.2, to achieve a better fit.

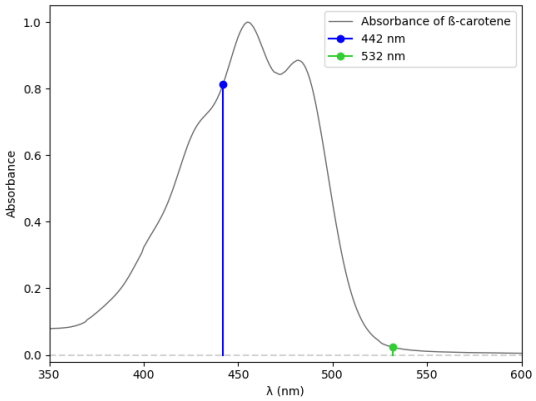


Figure 5.1: Absorption spectrum of β-carotene in acetone with indicated wavelength 442 nm and 532 nm used for Raman scattering measurements in this work.

## 5.8 Processing of spectral maps and spectra of organisms

The measured data were processed using the program WITec Project 6.0. After automatic cosmic spikes removal and shape background subtraction, multivariate decomposition was applied to obtain maps of pure chemical components.

The maps of fluorescence were obtained from data, where instead of shape background subtraction, constant background subtraction was employed to preserve the fluorescence. The fluorescence maps were created by using the quick filter function. This creates an intensity map of the chosen spectral region.

From the spectral stitching spectra, cosmic spikes were removed and constant background subtracted. The spectra were fitted in Python using a sum of Gaussian functions as described in Eq. 5.2. In some cases, a sum of three Gaussian functions was used, analogous to Eq. 5.2, to achieve a better fit.

## 5.9 Fluorescecne lifetime imaging (FLIM)

FLIM measurements and processing were conducted in collaboration with RNDr. Pavel Malý, Ph.D. from the Department of Biophysics, Institute of Physics, Faculty of Mathematics and Physics, Charles University. FLIM was performed using a confocal fluorescence microscope (iX83 with FV1200 scanner, Olympus) equipped with a UPlanSApo 60x water immersion objective (Olympus, NA = 1.2). Fluorescence detection was achieved through a confocal pinhole at a descanned port using a cooled hybrid photomultiplier tube (PMA Hybrid 40, PicoQuant), and photon counting was performed by a Time-Correlated Single Photon Counting (TCSPC) module (TimeHarp, PicoQuant).

Excitation was provided by a custom-made photonic crystal fiber (PCF) developed in collaboration with Photonics Bretagne, detailed in the Methods section. The PCF was pumped by a Ti oscillator (Chameleon Ultra II, Coherent), producing a spectrum ranging from 400 nm to 1000 nm. The desired spectral range was selected using a short-pass filter, with an excitation range of 460 nm to 510 nm, peaking at 490 nm. The detected emission, within the green region of visible

light, was obtained using a set of filters: a 514 nm long pass, a 560 nm short pass, and a 534/30 nm bandpass filter.

## 5.10 Widefield fluorescence microscopy

Microphotography acquisition was performed using an Olympus Provis AX70 microscope equipped with a fluorescent block (U-MWU, U-MWIB, U-MWG).

# 6. Results and discussion

## 6.1 Carotenoids in different solvents

### 6.1.1 Absorbtion of β-carotene

The absorption spectra of β-carotene in various solvents were measured and are depicted in Fig. 6.1. Due to the differing solubilities of β-carotene in these solvents, two different concentrations were used: 100 mg/L (186 µM) for hexane, chloroform (TCM), tetrahydrofuran (THF), and mineral oil (Min. oil), and 33 mg/L (62 µM) for acetic acid (AcetAc), acetone, and ethanol (EtOH). The spectra obtained with the higher concentration were divided by a factor of 3 to match the concentration levels for comparison in Fig. 6.1 and Tab.6.1.

As discussed previously (chapter 3.1.1), the observed absorption corresponds to the transition from the ground state ($S_0$) to the second singlet excited state ($S_2$), as the transition to the first singlet excited state ($S_1$) is symmetrically forbidden. The spectra show a distinctive three-peak pattern, which is characteristic of carotenoids and corresponds to the lowest three vibronic bands of the electronic transition. These bands are labeled as 0–0, 0–1, and 0–2 in Fig. 6.1 [Llansola-Portoles et al., 2017].

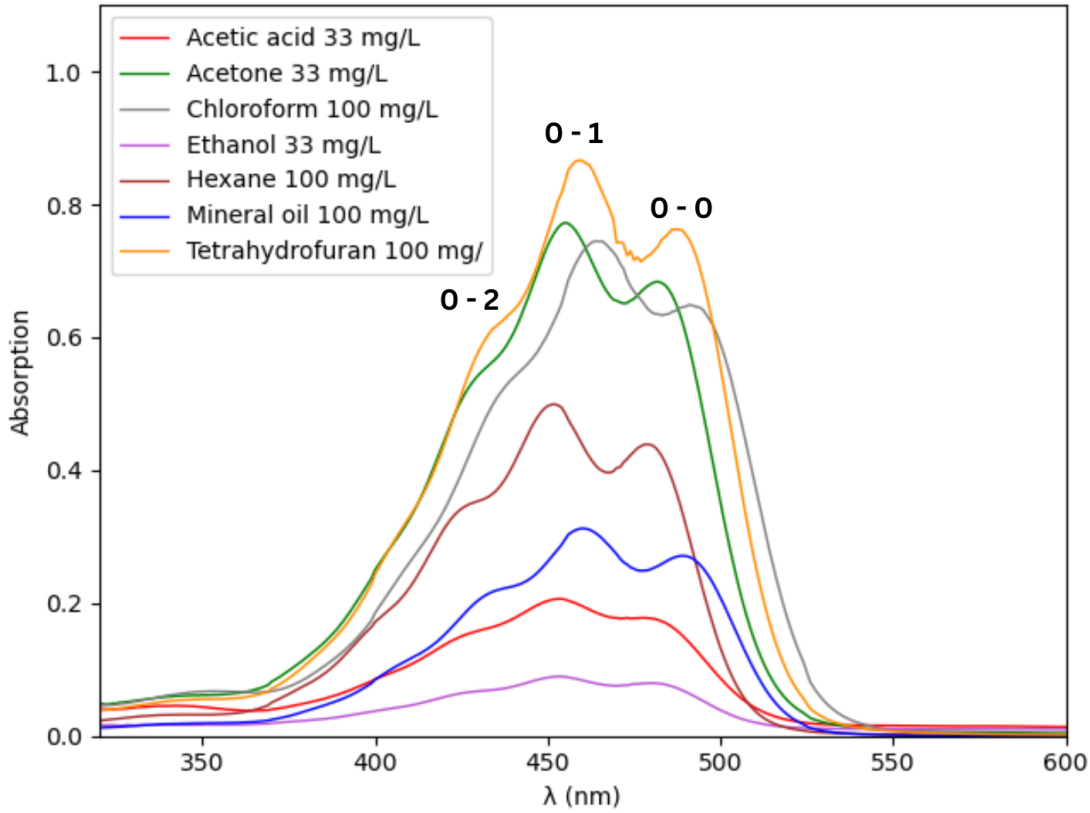


Figure 6.1: Absorbance of β-carotene in differnt solvents.

The first two columns of Tab. 6.1 summarize the results of the absorption measurements from Fig. 6.1, presenting the absorption maximum and its position. The subsequent three columns contain published values of absorptivity and

solubility for β-carotene from Craft and Soares [1992], along with refractive index data from Sigma-Aldrich (except for mineral oil, where the data is sourced from Avantar). Unfortunately, data on absorptivity and solubility for mineral oil and acetic acid were not found. Interestingly, the absorption intensity does not correlate with the reported values of absorptivity but aligns well with solubility, except for acetone. Excluding ethanol, all the concentrations of the reported solvents are significantly lower than their saturated solutions; thus, all the β-carotene should be dissolved, and solubility should not impact the absorption intensity.

Honda et al. [2018] investigated the impact of isomer content of β-carotene and astaxanthin on their solubility in hexane, ethanol, and acetone. They found that (all-E)-carotenoids are present in the crystal state, while the Z-isomers are in an amorphous state. Consequently, a higher content of Z-isomers leads to better solubility in all three solvents. For example, the solubility in ethanol of β-carotene containing 89.8 % Z-isomer is 250 times higher than that of the all-E-isomer. However, the degree of solubility enhancement varied for each solvent. Given that the β-carotene used in Fig. 6.1 was a mixture of isomers, its solubility may differ significantly from reported values. This is supported by Zang et al. [1997], who report that the absorbance of β-carotene in methanol increases linearly at lower concentrations, up to 5 mM, but shows a nonlinear increase at higher concentrations. This suggests that β-carotene may begin to form microcrystals at concentrations as low as 3 mg/L in methanol despite its reported solubility of 10 mg/L in this solvent. A similar effect might be observed in the spectra in Fig. 6.1, where solvents with higher solubility contain more dissolved β-carotene.

Another factor that could impact the absorption intensity is that the absorption of the 100 mg/L solutions might exceed the limit where absorption is linearly dependent on concentration. To further investigate this, more dilute solutions would need to be measured.

Bondarev and Knyukshto [1994] observed a bathochromic shift in the absorption of β-carotene with an increase in the solvent's refractive index. While the positions of the absorption maxima in the first column of Tab. 6.1 do not precisely correlate with the refractive indices presented in the last column, a trend is evident: solvents with higher refractive indices (between 1.41 and 1.47) exhibit shifts toward longer wavelengths (459 nm to 464 nm).

Table 6.1: Measured absorption intensity and position of absorption maximum. * reported molar absorptivity and solubility according to Craft and Soares [1992]. ** reported refractive indices according to Sigma-Aldrich, Avantar.

| | Absorption maximum (nm) | Absorption intensity (a.u.) | Molar absorptivity* (L mol$^{-1}$ cm$^{-1}$) | Solubility* (mg/L) | refractive index** 20 °C |
|---|---|---|---|---|---|
| Acetone | 455 | 0.77 | 137 400 | 200 | 1.36 |
| EtOH | 454 | 0.09 | 135 800 | 30 | 1.36 |
| AcetAc | 454 | 0.21 | | | 1.37 |
| Hexane | 452 | 0.50 | 139 200 | 600 | 1.38 |
| THF | 459 | 0.87 | 128 800 | 10 000 | 1.41 |
| TCM | 464 | 0.74 | 125 100 | 2 000 | 1.45 |
| Min. oil | 460 | 0.31 | | | 1.47 |

## 6.2 Fluorescence spectra of β-carotene

The fluorescence spectra of β-carotene in various solvents and concentrations were measured using two different purities, 93%, and 95%. The excitation wavelength was 442 nm, and the power was 3.6 mW. These spectra are depicted in Fig. 6.2. Most spectra exhibit intense fluorescence peaks in the green region around 530 nm (Fluo1). However, the spectrum of β-carotene with 95% purity in acetic acid (Fig. 6.2c) and chloroform (Fig. 6.2d) lacks this peak, instead showing a broader fluorescence peak around 650 nm (Fluo2). This peak, although of lower intensity compared to Fluo1, is also observed in 33 mg/L acetic acid (Fig. 6.2a), 20 mg/L acetone (Fig. 6.2c), chloroform at other concentrations (Fig. 6.2a, 6.2b), 20 mg/L ethanol (Fig. 6.2c), and 100 mg/L ethanol with 93% β-carotene (Fig. 6.2b). The positions and intensities of both fluorescence peaks are summarized in Tab. 6.2.

Van Riel et al. [1983] measured the fluorescence of β-carotene in chloroform and ethanol, finding fluorescence maxima at 540 nm and 527 nm, respectively, which align well with the measured values. Bondarev and Knyukshto [1994] observed a bathochromic shift in the fluorescence of β-carotene with an increase in the solvent's refractive index. Similar to absorption, solvents with higher refractive indices, such as tetrahydrofuran, chloroform, and mineral oil (ranging from 1.41 to 1.47), exhibit shifts toward longer wavelengths (536 nm to 545 nm). Despite variations in the measured emission of β-carotene in different solvents and the reported fluorescence maxima by different authors, the emission consistently falls within the green region of the spectrum. This consistency supports the hypothesis that carotenoids could be responsible for GAF in some biological objects.

The peak around 650 nm is likely due to the fluorescence of undissolved β-carotene, as it predominantly appears in more polar solvents such as acetic acid, acetone, and ethanol. The presence of this peak in chloroform is rather unusual, given that its solubility, according to Craft and Soares [1992], is the second highest (after THF) among the solvents used in this study. However, chloroform, despite

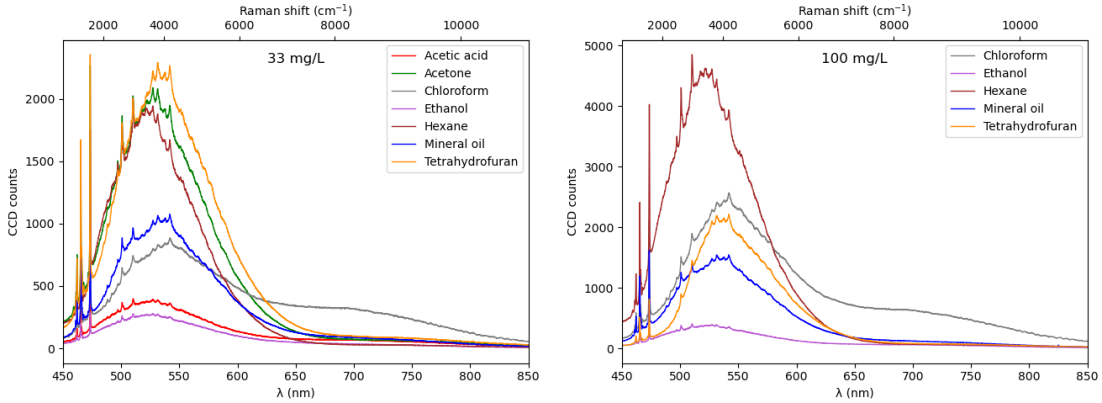


(a) purity 93 %




(b) purity 93 %

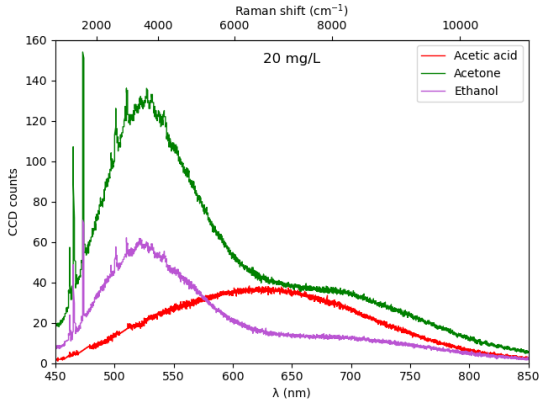


(c) purity 95 %

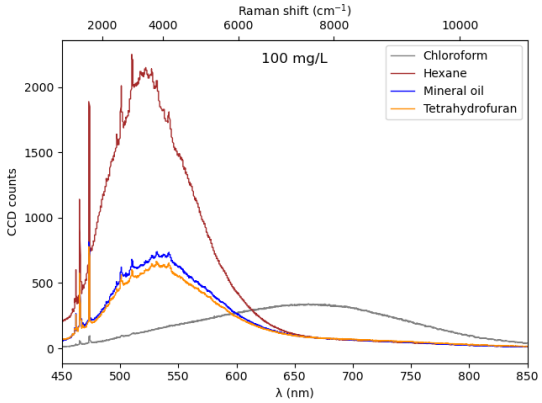


(d) purity 95 %

Figure 6.2: Fluorescence of β-carotene in different solvents and concentrations under 442 nm excitation with a power of 3.6 mW was measured using the spectral stitching method. The spectra exhibit the Raman signal of β-carotene visible as very narrow lines in the spectral region 450 - 550 nm. Overtone and combination vibrations are also present.

its high solubility for β-carotene, is quite a polar solvent, and β-carotene typically does not dissolve well in polar solvents.

The Tab. 6.3 contains the intensities after fluorescence subtraction and positions of two prominent Raman bands of carotenoids ($\nu_1$ and $\nu_2$) as well as the Fluo1 to $\nu_1$ intensity ratio. For all solvents except hexane and tetrahydrofuran (THF), the ratios are around 1, indicating similar intensities for $\nu_1$ and fluorescence in most solvents. In hexane, fluorescence appears more intense than the Raman signals. In THF at 100 mg/L, fluorescence is three times higher than the Raman signals. The positions of $\nu_2$ remain constant across different solvents. Only chloroform with 95% β-carotene ( in Tab. 6.3 indicated as TCM 100*) shows markedly different values for both $\nu_1$ and $\nu_2$, attributed to very low intensity, as seen in Fig. 6.2d. The vibration $\nu_1$ appears more sensitive to the environment, even though the differences are still very small, with values ranging from 1524 $cm^{-1}$ to 1527 $cm^{-1}$. Interestingly, solvents with higher refractive indices—chloroform, mineral oil, and tetrahydrofuran—exhibit lower wavenumbers (1524 $cm^{-1}$).

Table 6.2: Fluorescence of β-carotene in different solvents and concentrations.The * symbol indicates the purity of 95%. Fluo1 indicates a fluorescence peak with a maximum of around 530 nm and Fluo2 fluorescence peak with a maximum of around 650 nm.

| | c (mg/L) | Fluo1 (nm) | Fluo1 (cts) | Fluo2 (nm) | Fluo2 (cts) |
|---|---|---|---|---|---|
| AcetAc | 33 | 525 | 333 | 651 | 77 |
| | 20* | | | 627 | 37 |
| Acetone | 33 | 531 | 1875 | | |
| | 20* | 524 | 108 | 644 | 40 |
| TCM | 33 | 536 | 682 | 666 | 334 |
| | 100 | 540 | 1951 | 650 | 704 |
| | 100* | | | 656 | 334 |
| EtOH | 33 | 530 | 234 | | |
| | 100 | 525 | 331 | 644 | 74 |
| | 100* | 524 | 50 | 645 | 14 |
| Hexane | 33 | 526 | 1788 | | |
| | 100 | 525 | 4289 | | |
| | 100* | 525 | 1964 | | |
| Min. oil | 33 | 537 | 929 | | |
| | 100 | 537 | 1343 | | |
| | 100* | 536 | 642 | | |
| THF | 33 | 537 | 2038 | | |
| | 100 | 545 | 1963 | | |
| | 100* | 536 | 562 | | |

Table 6.3: Raman spectra of β-carotene in different solvents and concentrations. The last column contains the ratio between the intensity of Fluo1 and $\nu_1$. The * symbol indicates the purity of 95%.

| | c (mg/L) | $\nu_1$ ($cm^{-1}$) | $\nu_1$ (cts) | $\nu_2$ ($cm^{-1}$) | $\nu_2$ (cts) | Fluo1:$\nu_1$ ratio |
|---|---|---|---|---|---|---|
| AcetAc | 33 | 1157 | 288 | 1527 | 201 | 1.2 |
| | 20* | | | | | |
| Acetone | 33 | 1156 | 1643 | 1526 | 1169 | 1.1 |
| | 20* | 1157 | 103 | 1526 | 72 | 1.0 |
| TCM | 33 | 1157 | 727 | 1524 | 420 | 0.9 |
| | 100 | 1157 | 950 | 1524 | 704 | 1.2 |
| | 100* | 1160 | 55 | 1543 | 29 | |
| EtOH | 33 | 1157 | 174 | 1526 | 124 | 1.3 |
| | 100 | 1157 | 320 | 1526 | 228 | 1.0 |
| | 20* | 1156 | 49 | 1527 | 34 | 1.0 |
| Hexane | 33 | 1157 | 1148 | 1527 | 765 | 1.6 |
| | 100 | 1157 | 2582 | 1527 | 1566 | 1.7 |
| | 100* | 1157 | 1230 | 1527 | 738 | 1.6 |
| Min. oil | 33 | 1157 | 894 | 1524 | 650 | 1.0 |
| | 100 | 1157 | 1238 | 1524 | 891 | 1.1 |
| | 100* | 1157 | 612 | 1524 | 426 | 1.0 |
| THF | 33 | 1156 | 1837 | 1524 | 1272 | 1.1 |
| | 100 | 1156 | 643 | 1524 | 393 | 3.1 |
| | 100* | 1156 | 600 | 1524 | 432 | 0.9 |

### 6.2.1 Concentration series of β-carotene in hexane and mineral oil

Mineral oil and hexane were selected to measure the dependency of Raman intensity and fluorescence on concentration under excitation 442 nm and power 3.6 mW. The spectra are depicted in Fig. 6.3. The dependencies of fluorescence intensity, the two main Raman band intensities, and the fluorescence:$\nu_1$ intensity ratio on concentration are shown in Fig. 6.4. In hexane, the fluorescence intensity does not increase linearly with concentration within the measured range; the curve in Fig. 6.4a appears saturated, and the spectra for 160 μM and 200 μM in Fig. 6.3b overlap. The highest concentration, 200 μM, corresponds to 107 mg/L, which is almost six times lower than the solubility reported by Craft and Soares [1992]. However, as discussed in Chapter 6.1.1, actual solubilities are difficult to predict.

The fluorescence to $\nu_1$ Raman band ratio (Fig. 6.4c) indicates that fluorescence in hexane has a higher relative intensity than in mineral oil, as already shown in Tab. 6.3. Another notable difference is that in mineral oil, the ratio increases very slightly and remains almost constant, whereas in hexane, there is a noticeable increase, especially between 40 and 120 μM. The fluorescence intensity thus rises more quickly with concentration than the Raman band intensity. The

concentration limit for detecting β-carotene fluorescence is in the order of lower tens of µM (10 µM = 5.4 mg/L).

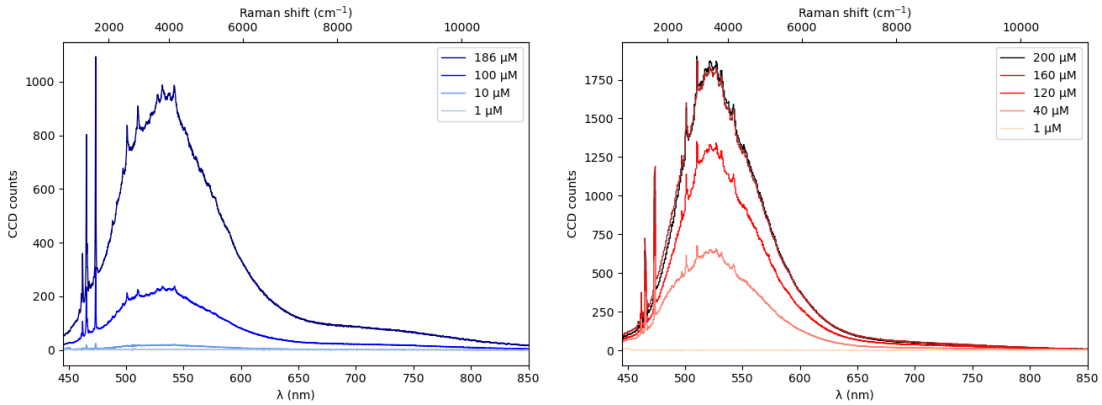


(a) Mineral oil (b) Hexane

Figure 6.3: Concentration series of β-carotene in mineral oil and hexane under 442 nm excitation and power 3.6 mW.

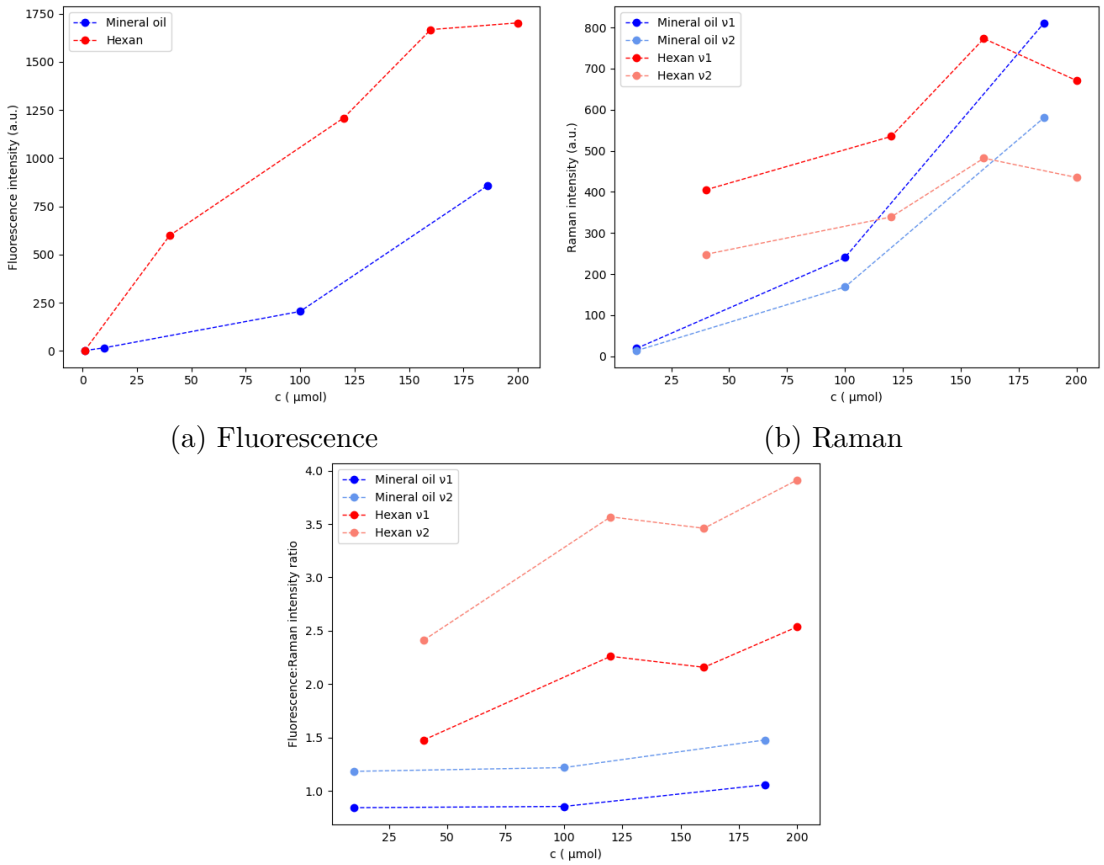


(a) Fluorescence (b) Raman

(c) Fluorescence:$\nu_1$ ratio

Figure 6.4: Fluorescence and Raman intensity dependency on concentration.

### 6.2.2 Fluorescence spectra of Astaxanthin

Fluorescence spectra of astaxanthin in various solvents under blue excitation (442 nm) and power 3.6 mW are depicted in Fig. 6.5, with the characteristics summarized in Tab. 6.4. Astaxanthin did not dissolve in hexane and mineral oil, so data for these solvents are not included. The fluorescence maximum, Fluo1, is redshifted by approximately 30 nm compared to β-carotene. A bathochromic shift is observed in tetrahydrofuran (THF), which has a higher refractive index (1.41) compared to the other solvents (1.37 or 1.36). Similar to β-carotene, a second fluorescence peak is observed in acetic acid, with a fluorescence maximum at 667 nm, likely due to the fluorescence of undissolved astaxanthin.

Tab. 6.5 presents the intensities after fluorescence subtraction, the positions of two prominent Raman bands of carotenoids ($\nu_1$ and $\nu_2$), and the Fluo1 to $\nu_1$ intensity ratio. The Raman spectra of astaxanthin are even less sensitive to the environment than those of β-carotene. The positions of both $\nu_1$ and $\nu_2$ remain consistent across all solvents. The fluorescence to Raman ratios for astaxanthin differ significantly from those of β-carotene. While the ratios for β-carotene are around 1 or higher, for astaxanthin, the values decrease to as low as 0.5 in ethanol, and they do not reach 1 in any solvent. This indicates that the intensity of Raman bands is higher than the fluorescence in astaxanthin.

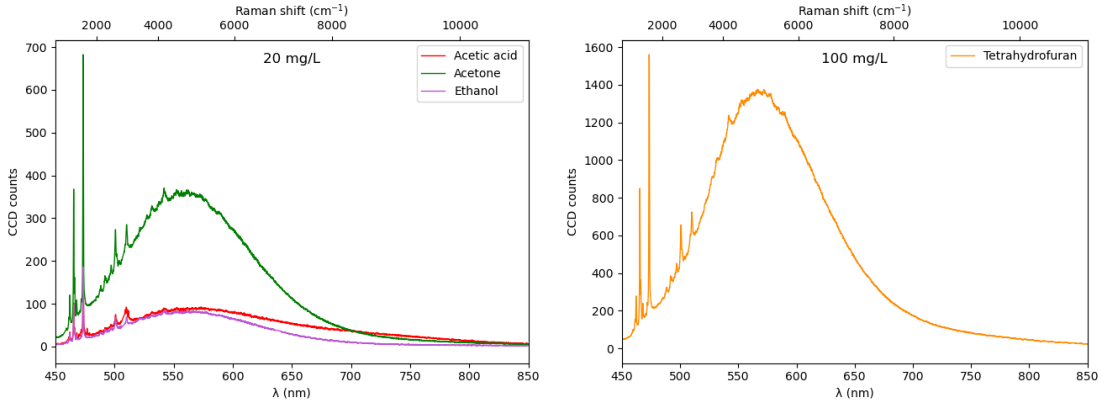


(a) (b)

Figure 6.5: Fluorescence of astaxanthin in different solvents and concentrations under 442 nm excitation with a power of 3.6 mW was measured using the spectral stitching method. The spectra exhibit the Raman signal of astaxanthin, including overtone and combination vibrations.

Table 6.4: Fluorescence of Astaxanthin in different solvents and concentrations. Fluo1 indicates fluorescence peak with maximum around 560 nm and Fluo2 fluorescence peak with maximum around 660 nm.

| | c (mg/L) | Fluo1 (nm) | Fluo1 (cts) | Fluo2 (nm) | Fluo2 (cts) |
|---|---|---|---|---|---|
| AcetAc | 20 | 556 | 71 | 667 | 35 |
| Acetone | 20 | 563 | 345 | | |
| EtOH | 20 | 565 | 78 | | |
| THF | 100 | 574 | 1272 | | |

Table 6.5: Raman spectra of astaxanthin in different solvents and concentrations. The last column contains the ratio between the intensity of Fluo1 and $\nu_1$.

| | c (mg/L) | $\nu_1$ ($cm^{-1}$) | $\nu_1$ (cts) | $\nu_2$ ($cm^{-1}$) | $\nu_2$ (cts) | Fluo1:$\nu_1$ ratio |
|---|---|---|---|---|---|---|
| AcetAc | 20 | 1524 | 163 | 1159 | 83 | 0.9 |
| Acetone | 20 | 1523 | 597 | 1158 | 308 | 0.6 |
| EtOH | 20 | 1523 | 167 | 1158 | 84 | 0.5 |
| THF | 100 | 1523 | 1370 | 1158 | 708 | 0.9 |

The transferability of these observations from solutions to living microorganisms can be challenging due to several factors. One primary reason is the limitation of commercially available carotenoids during our studies on solutions. However, cells contain a multitude of other carotenoids, as mentioned in Tables 4.1, 4.2, and 4.3. Some of these exotic carotenoids are hard to obtain, and there are so many of them that it is impossible to explore all within a single thesis, even if we had access to them. For instance, in *Rhodotorula glutinis* [Buzzini et al., 2007], besides the commonly studied $\beta$-carotene, the carotenoids torularhodin and torulene are present in significant amounts, constituting 46.8% and 30.6% of the total carotenoids, respectively (Tab. 4.2). Similarly, in *Vischeria/Eustigmatos* strains [Stoyneva-Gärtner et al., 2019], apart from the high percentage of $\beta$-carotene (up to 29%), violaxanthin is also present in substantial amounts up to 32% (Tab. 4.1). The diversity and interactions of these carotenoids within the cellular environment can lead to different behaviors compared to isolated solutions. These interactions and the cellular matrix can significantly influence the solubility, stability, and functionality of carotenoids, making direct comparisons challenging. Therefore, while studying additional carotenoids in solution might provide some insights, the complexity and diversity within the cells highlight the limitations of transferring observations directly from solutions to living microorganisms.

## 6.3 Carotenoids in organisms

### 6.3.1 *Vischeria* sp.

*Vischeria* sp., shown in Fig. 6.6, was imaged using a widefield fluorescence microscope with blue excitation. In the fluorescence image (Fig. 6.6b), one can easily distinguish the reddish globule, which exhibits yellow fluorescence, the plastid with red fluorescence from chlorophyll, and the green fluorescence of interest, which likely comes from lipid droplets.

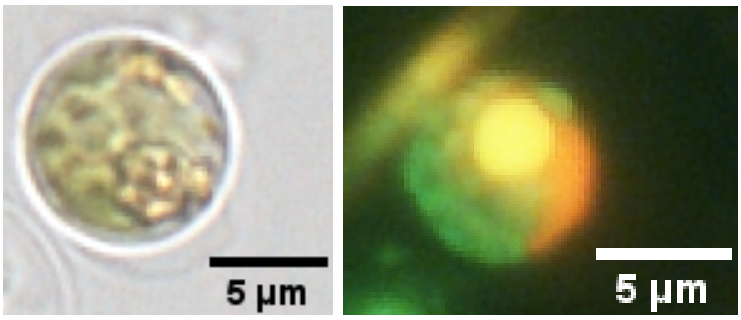


(a) Brigthfield (b) Fluorescence

Figure 6.6: Two different *Vischeria* sp. cells imaged with a widefield fluorescence microscope, one in brightfield and one with blue excitation.

Spectral maps and spectra of *Vischeria* sp. obtained with green excitation (532 nm) are depicted in Fig. 6.7. Two laser powers were used: 20 µW for the detection of carotenoids and fluorescence to avoid bleaching them and higher power for the detection of other compounds with lower Raman signals than carotenoids. An interesting observation is that, at low power, two notably different Raman spectra of carotenoids were detected.

The first carotenoid spectrum colocalizes with the plastid, indicated as PL in Fig. 6.7. In the brightfield image, the plastid appears as a green area. The map showing chlorophyll fluorescence is indicated as Fluo 662 nm. This map shows increased fluorescence around 662 nm, which corresponds to the shoulder of chlorophyll fluorescence. In Fig. 6.7, in spectrum Fluo 662, the position of the spectral region used for the construction of the fluorescence map is highlighted with a blue band. The cellular structure providing another carotenoid Raman spectrum is colocalized with the yellow fluorescence of the reddish globule in map Fluo 590 nm. As seen in the spectrum Fluo 590 nm, this fluorescence is spectrally very broad, and the wavelength 590 nm lies approximately in the middle of this fluorescence band. Also, no carotenoid Raman bands are present in this region and cannot, therefore, account for the total intensity. This fluorescence even extends into the chlorophyll fluorescence region and is therefore also visible in the Fluo 662 nm map.

There are two main differences between the two observed Raman spectra of carotenoids in low power (20uW): the relative intensity of $\nu_1$ and $\nu_2$ and the shifted position of $\nu_1$. In the plastid, the intensity of $\nu_2$ is lower than that of $\nu_1$, whereas, in the reddish globule, both intensities are approximately the same. The $\nu_1$ peak occurs at 1524 $cm^{-1}$ in the plastid and at 1517 $cm^{-1}$ in the reddish globule. These differences suggest either the presence of two different carotenoids,

one predominantly in the plastid and the other in the reddish globule, or the same carotenoid existing in different environments.

Interestingly, *Vischeria* sp. is not the only organism where the phenomenon of two carotenoid spectra, one in the plastid and one in the reddish globule, is observed. Similar carotenoid spectra with the same features were distinguished in *Chromera* during other studies in our lab. This indicates that it is likely a more general feature, not necessarily specific just to one organism.

At higher power (10 mW), residues of another carotenoid (HP) are observed. This carotenoid exhibits characteristics between the two previously mentioned carotenoids. The $\nu_1$ peak has a frequency of 1521 $cm^{-1}$, which lies in between the positions of $\nu_1$ observed in plastid and reddish globule. The intensity of $\nu_2$ is similar to $\nu_1$. During the photobleaching of chlorophyll, the photooxidation of carotenoids present in plastids also occurs, which is why the signal of carotenoids in plastids is completely absent with higher power. Only carotenoids that have been somehow protected from reactive singlet oxygen and reactive oxygen species (ROS) produced during photobleaching can provide a Raman signal. This applies, in particular, to carotenoids dissolved in lipid droplets.

Vischeria sp. is known for its accumulation of oil droplets in the cells [She et al., 2022], which aligns with the detection of a lipid spectrum at high power. The spectrum certainly belongs to unsaturated lipids, as it exhibits intense vibration at 1657 $cm^{-1}$, which is assigned to the C=C stretching mode of fatty acids and lipids Wu et al. [2011]. Also, other markers for the presence of unsaturated fatty acids were identified: the peak at 1264 $cm^{-1}$ corresponds to the =C—H cis stretch and the =C—H stretch at 3011 $cm^{-1}$. The average number of C=C bonds can be estimated from the intensity ratios of peaks at 1657 $cm^{-1}$ ($I_{1650}$) and 1442 $cm^{-1}$ ($I_{1440}$) using a linear equation reported by Wu et al. [2011]:

$$y = 0.67x + 0.10, \tag{6.1}$$

where $y$ represents $I_{1650}/I_{1440}$ intensity ratio and $x$ the average number of C=C bonds. Applying eq. 6.1 to the Raman spectrum of lipids in *Vischeria* sp., a number 2.06 is obtained, meaning that the average number of double bonds is two. By comparing the shape of the spectra to Raman spectra of 11 pure fatty acids reported by Wu et al. [2011], and regarding the number of double bonds, the lipid spectrum can be attributed to linoleic acid with a chain of 18 carbons and two double bonds. The Raman spectrum of lipids contains a peak at 1582 $cm^{-1}$, which cannot be attributed to lipids. This vibration origins probably from retinol or some compound derived from retinol. This will be further discussed in the section about *Haeamatococcus* 6.3.3, where it was possible to demix this compound from lipids and further analyze it.

Furthermore, the characteristic Raman bands of guanine crystals were detected in the spectra of *Vischeria* sp. It has been reported that *Vischeria* sp. accumulates guanine, likely using it as a nitrogen source [Mojzeš et al., 2020]. The last observed component is the Raman spectrum of the reddish globule. Because this spectral component was extracted from areas of cells with a high fluorescence background, it is burdened by higher stochastic noise and artifacts caused by the etalon effect of the CCD detector [Optical Etaloning Web resource]. The spectrum itself contains Raman bands showing the presence of $CH_2$ groups (deformation band of $CH_2$ groups at 1442 $cm^{-1}$, CH stretching bands at 2700-3100

$cm^{-1}$), but the low quality of the spectrum does not allow a closer identification of the chemical composition.

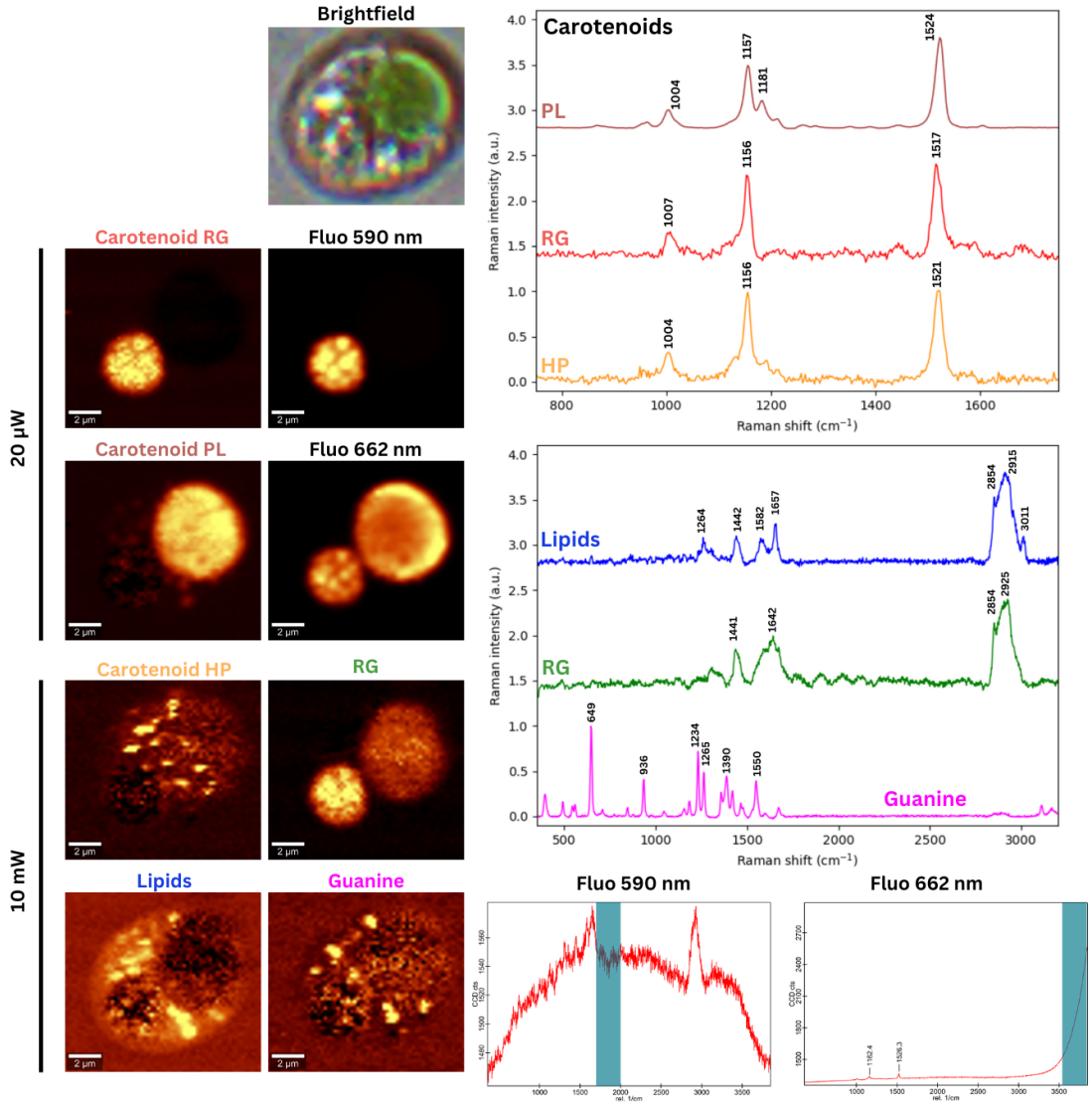


Figure 6.7: Spectral maps and spectra of *Vischeria* sp. obtained with green excitation (532 nm) and two laser powers 20 µW and 10 mW. Tree types of carotenoids were found: Plastid (PL), Reddish globule (RG) and High power (HP).

Chemical maps and spectra obtained using blue excitation at 442 nm are depicted in Fig. 6.8. Only one component, the carotenoid, was found under blue excitation. In this case, the Raman signal is strongly increased due to resonance effectively covering the signals of other substances. Interestingly, only one type of carotenoid was observed, and its spectrum is similar to those of the carotenoid in the plastid under 532 nm excitation. The carotenoid from the reddish globule is absent, likely due to the strong yellow fluorescence of the reddish globule (see Fig. 6.6b). This fluorescence causes significant interference, making the carotenoid signal difficult to detect even after background subtraction, resulting in noisy spectra. Also, reabsorption of the Raman signal is more pronounced in the blue region than in the green region [Lu et al., 2018]. This effect is especially significant

because the reddish globule typically resides in the central region of the cell. Consequently, the yellow fluorescence emitted by the reddish globule experiences less absorption compared to the Raman signal, making it more observable. In addition to the signals described under green excitation, the carotenoid spectrum observed under blue excitation shows two peaks around 3000 $cm^{-1}$. These peaks correspond to combination and overtone vibrations: 2678 $cm^{-1}$ corresponds to $\nu_1 + \nu_2$ and 3055 $cm^{-1}$ to $2 * \nu_1$.

Apart from the carotenoid chemical map, two fluorescence maps are shown in Fig. 6.8. The first map displays fluorescence intensity around 528 nm *i.e.* with the maximum in the green spectral region (Fluo 528 nm), as highlighted with the blue band in the Fluo 528 nm spectrum. This value is very close to the fluorescence maximum of β-carotene measured in different solvents in section 6.2. The broad yellow fluorescence of the reddish globule extends into this green region and can be clearly observed in this fluorescence map. Excluding the fluorescence from the reddish globule, the distribution of fluorescence around 528 nm correlates well with the distribution of carotenoids deduced from their Raman signal.

The second fluorescence map shown in Fig. 6.8 corresponds to the distribution of residual chlorophyll fluorescence (Fluo 684 nm), measured after low-power Raman mapping of the carotenoid distribution, indicating partial bleaching of the chlorophyll. One may notice the different localization of plastids in the cells shown in Fig. 6.8 and Fig. 6.7. Really, A notable difference is observed between the distribution of plastids measured under green excitation (Fig. 6.7) and those measured under blue excitation (Fig. 6.8). At this point, it should be emphasized that due to the fact that experiments with different excitations were performed at different times, it was not possible to ensure that the measured cultures were at the same developmental stage. Under blue excitation, the plastids are shrunken towards the cell periphery, corresponding to a later growth stage where the cell is predominantly filled with lipids. This difference is also evident in the brightfield images (Figs. 6.7 and 6.8), where the cells used for measurement under blue excitation exhibit more yellowish tones.

On the bright field image shown in Fig. 6.8, the locations where the fluorescence spectra were taken are marked with the color crosses. The corresponding fluorescence spectra are shown in lower panels and labeled using the same color code. The positions and full widths at half maximum (FWHM) of fitted Gaussians are indicated in the measured spectra. The first spectrum, denoted by the blue cross and labeled as "Blue" in Fig. 6.18, exhibits a maximum at 680 nm, corresponding to chlorophyll fluorescence Lamb et al. [2018]. This measurement was taken from the brightest area in the Fluo 684 nm map. The "Green" spectrum, likely corresponding to carotenoids, was collected at a bright spot in the carotenoid map, with a maximum of 538 nm. This spectrum also displays the strongest Raman signal of carotenoids. Some chlorophyll fluorescence is also mixed in.

The "Cyan" spectrum, obtained from the reddish globule of the first cell (easily identifiable on the Fluo 528 nm map), shows green fluorescence with a maximum at 544 nm and broad yellow fluorescence with a maximum at 605 nm. The "Red" spectrum represents a mixture of all fluorescence bands discussed before. The Gaussian peaks in the "Cyan" and "Green" spectra, with maxima in the green region at 544 nm and 538 nm, respectively, are very similar. Apart from the

maxima position, the FWHM are also closely aligned. Moreover, the position of these Gaussian peaks corresponds well with the emission maxima of β-carotene in solvents with higher refractive indices (chloroform, mineral oil, tetrahydrofuran) presented in section 6.2.

FLIM of *Vischeria* sp., depicted in Fig. 6.9, revealed that the fluorescence lifetime in the green region is extremely short on the subnanosecond scale. This is a comparable timescale to the values reported very recently by Solovchenko et al. [2024]. They measured fluorescence lifetimes in cells of the microalga *Bracteacoccus aggregatus* using FLIM with 750 nm two-photon excitation, showing that lifetimes ranged from 200 ps to approximately 1200 ps in chloroplasts and from 250 ps to 1000 ps in oleosomes, depending on the cell stage. The shorter lifetimes were attributed to primary carotenoids, present mostly in the green stage, while the longer ones were attributed to secondary carotenoids observed mostly in the later red stage. Similarly, Grudzinski et al. [2018] conducted FLIM measurements under 470 nm excitation in human colon epithelial cells and colon adenocarcinoma cells. The analysis of the fluorescence signal from cells cultured in a medium supplemented with exogenous carotenoids, lutein, or zeaxanthin revealed an additional, relatively short lifetime component of 300 ps. This component was attributed to carotenoids and is comparable to lifetimes measured in *Vischeria* sp.. These findings support the hypothesis that green autofluorescence (GAF) originates from carotenoids.

It is noteworthy that the fluorescence lifetime of the reddish globule is shorter than that of other cellular components. This suggests that the two carotenoids (or one carotenoid in different environments) differ not only in Raman spectra but also in fluorescence lifetime. Another possibility is that the broad yellow fluorescence from the reddish globule, whose shoulder reaches the measured region, has such a short lifetime.

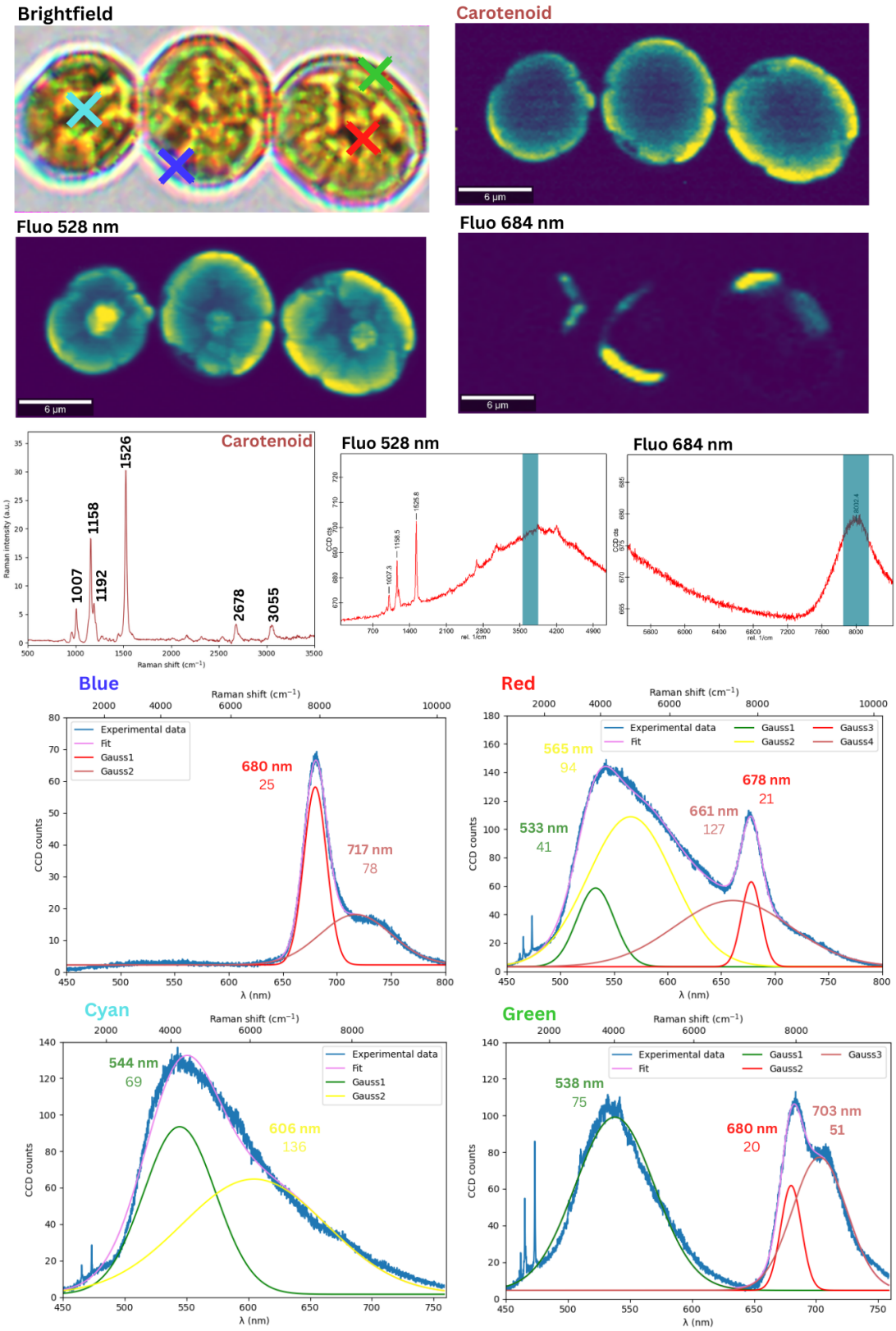


Figure 6.8: Raman maps and spectra of *Vischeria* sp. obtained with blue excitation (442 nm). The maps highlight the distribution of carotenoids and fluorescence across the cells. Spectral stitching spectra (Blue, Red, Cyan, Green), recorded at places marked with a cross in the brightfield image, are also shown. The spectra were fitted using the sum of Gaussians. The position of these Gaussians and the full width at half maximum (FWHM) are written in each graph.

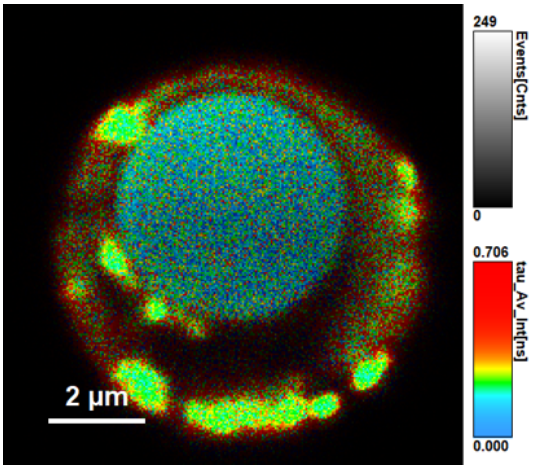


Figure 6.9: Fluorescence lifetime imaging (FLIM) of *Vischeria* sp., showing variations in fluorescence lifetimes between different cellular components.

### 6.3.2 *Rhodotorula glutinis*

*Rhodotorula glutinis*, shown in Fig. 6.10, was imaged using a widefield fluorescence microscope with blue excitation. From the fluorescence image Fig. 6.10b, it is evident that *R. glutinis* has a yellow fluorescence background, which interferes with the green fluorescence of our interest. The white arrows indicate cells where the studied green fluorescence is more apparent.

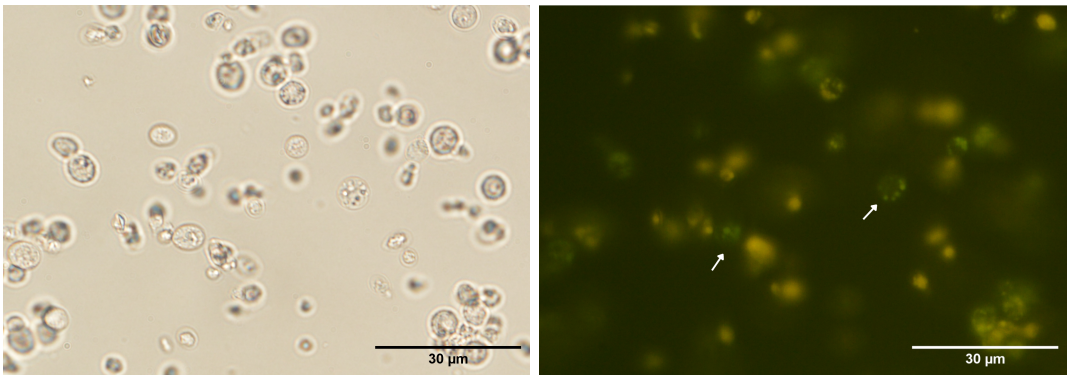


(a) Brigthfield (b) Fluorescence

Figure 6.10: *R. glutinis* imaged with a widefield fluorescence microscope in brightfield and fluorescence contrast with blue excitation. White arrows indicate cells with the green fluorescence of interest.

Spectral maps and spectra of *R. glutinis* obtained with green excitation (532 nm) are depicted in Fig. 6.11. Two laser powers were used: a low power of 100 µW for the detection of carotenoids and fluorescence to avoid bleaching and a higher power of 32 mW for the detection of other compounds with lower signals than carotenoids. In *R. glutinis*, only one other compound apart from carotenoids was found - lipids. The vibration at 1655 $cm^{-1}$ assigned to C=C stretching is less intense compared to *Vischeria* sp.. Applying eq. 6.1 on the intensity ratio of the bands at 1655 $cm^{-1}$ and 1450 $cm^{-1}$ in lipids Raman spectrum of *R. glutinis*, a

value of 0.53 is obtained, indicating a mixture of saturated and one double-bond fatty acids.

Carotenoids in *R. glutinis* exhibit vibrational modes at $\nu_1 = 1509$ cm$^{-1}$, $\nu_2 = 1152$ cm$^{-1}$, and $\nu_3 = 1001$ cm$^{-1}$. Interestingly, unlike in solvents and *Vischeria* sp. plastids, where $\nu_1$ is the most intense vibration, in *R. glutinis* the $\nu_2$ band is the most intense. This observation of carotenoids and lipids is consistent with the findings of Pacia et al. [2016], who studied a different strain, *Rhodotorula mucilaginosa*, under various cultivation conditions using Raman microscopy with the same excitation wavelength (532 nm). They detected lipids and carotenoids with vibrational positions at $\nu_1 = 1512$ cm$^{-1}$ and $\nu_2 = 1155$ cm$^{-1}$ in yeast cultivated under aerobic conditions, the same conditions used in this study. These positions closely match the measured values.

Spectral map Fluo 590 nm (Fig. 6.11) shows the distribution of increased background around 590 nm, as indicated in spectrum Fluo 590 nm with a blue band. This map looks almost identical to the carotenoid map obtained with an excitation power of power 100 μW. The distribution of carotenoids correlates with the distribution of increased background, which is, therefore, likely caused by the carotenoids. As discussed in section 5.7, excitation of 532 nm is still slightly absorbed by carotenoids and may thus cause a fluorescence background.

Comparing the two maps obtained with higher laser power, it is observed that the bright spots in the carotenoid map overlap with the dark spots in the lipids map. This phenomenon occurs because the signal from carotenoids masks the signals from lipids. However, at higher power levels, the carotenoids bleach, gradually revealing the signal from the underlying lipid droplets. Despite this bleaching effect, there is still a well-observed spatial correlation between the distribution of lipids (as visible in the high-power Raman map) and unbleached carotenoids (as seen in the Raman map obtained upon low-power excitation of 100 μW).

Spectral maps and spectra obtained using blue excitation (442 nm) are depicted in Fig. 6.12. Similar to *Vischeria* sp., only one component, the carotenoid, was found under blue excitation. When we compare this spectrum with the carotenoid spectrum obtained under green excitation (532 nm), it is evident that the most intense peak under blue excitation is $\nu_1$, not $\nu_2$. Additionally, the position of $\nu_1$ is significantly shifted from 1509 cm$^{-1}$ under green excitation to 1521 cm$^{-1}$ under blue excitation. The positions of $\nu_2$ at 1156 cm$^{-1}$ and $\nu_3$ at 1005 cm$^{-1}$ are closer to those observed under green excitation. The combination vibration $\nu_1 + \nu_2$ is observed at 2671 cm$^{-1}$, and the overtone vibration $2 \times \nu_1$ appears at 3032 cm$^{-1}$.

One possible explanation for the difference in the position of $\nu_1$ might be attributed to the carotenoid content in *R. glutinis*. The main carotenoids in this yeast are β-carotene, torulene, and torularhodin [Buzzini et al., 2007]. The absorption of torulene and torularhodin is redshifted by approximately 40 nm compared to β-carotene [Mot et al., 2017]. Therefore, the Raman spectra of torulene and torularhodin will be more resonantly enhanced at 532 nm than β-carotene. Conversely, β-carotene is more resonantly enhanced under blue excitation.

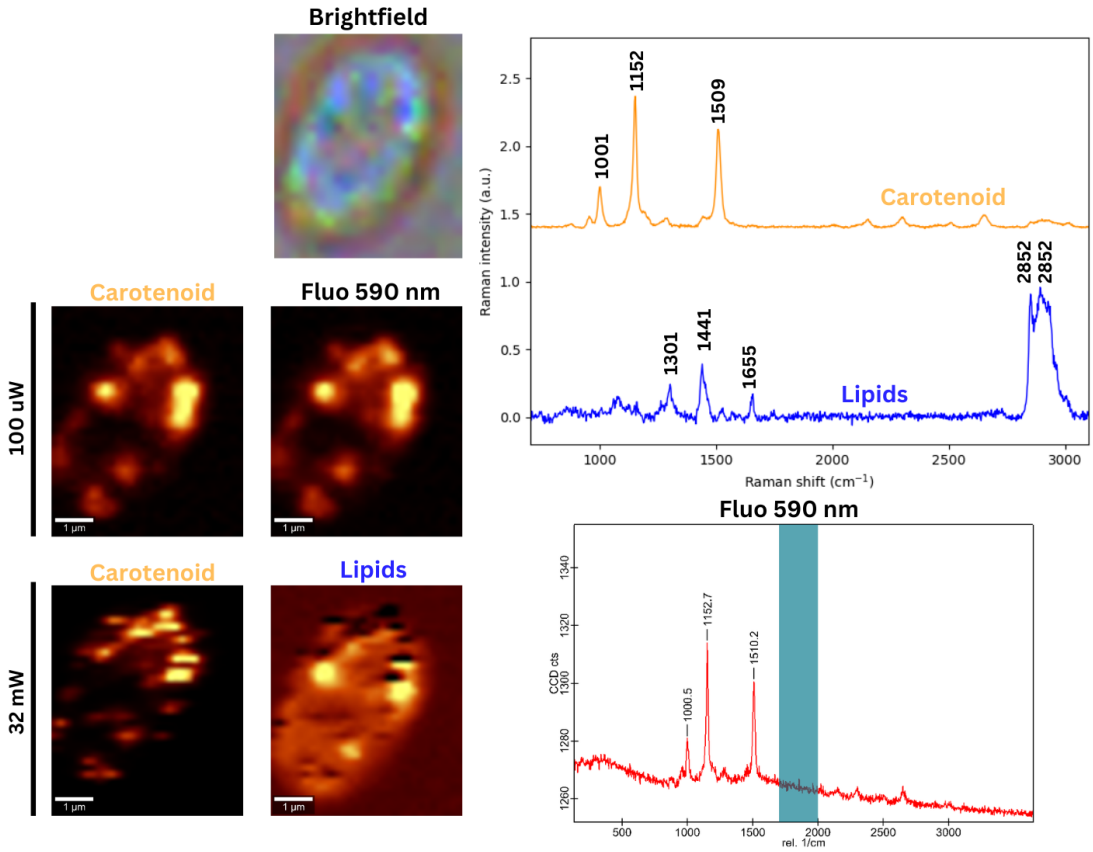


Figure 6.11: Spectral maps and spectra of *R. glutinis* obtained with green excitation (532 nm) at two laser powers: 100 µW and 32 mW.

Furthermore, Mot et al. [2017] studied the carotenoids from *Rhodotorula mucilaginosa*, analyzing the fractions obtained from HPLC using a Raman spectrometer with an excitation wavelength of 532 nm. The carotenoid spectrum measured under green excitation in Fig. 6.7 closely matches the fraction identified as torulene, exhibiting vibrations at $\nu_2 = 1151$ cm$^{-1}$ and $\nu_1 = 1508$ cm$^{-1}$, which are very close to 1152 cm$^{-1}$ and 1509 cm$^{-1}$, respectively. The reported values for torularhodin are also very similar, with $\nu_1 = 1511$ cm$^{-1}$ and $\nu_2 = 1149$ cm$^{-1}$.

The carotenoid spectrum of *R. glutinis* measured under blue excitation is very similar to the vibrational positions measured for β-carotene in mineral oil, presented in section 6.2, where $\nu_3 = 1005$ cm$^{-1}$, $\nu_2 = 1157$ cm$^{-1}$, and $\nu_1 = 1524$ cm$^{-1}$. These values closely match the 1005 cm$^{-1}$, 1156 cm$^{-1}$, and 1521 cm$^{-1}$ vibrations measured in *R. glutinis*, indicating that β-carotene is more resonantly enhanced under blue excitation.

Comparing the distribution of carotenoid with the fluorescence distribution around 530 nm (Fluo 530 map and spectra in Fig 6.12), very good colocalization is observed, just as under green excitation.

Spectral stitching spectra from different cells were measured and are depicted in Fig. 6.12 (Cell 1 to Cell 6). The spectra were fitted with the sum of two Gaussian functions. The maxima and full widths at half maximum (FWHM) for these fits are indicated on each graph. Apart from fluorescence, the Raman signal of carotenoids is also detected in all cells except Cell 5. The signal in Cell 5 likely originates predominantly from the yellow background observed in Fig. 6.10b.

The green Gaussian maxima in cells 1, 2, 3, 4, and 6 lie between 502 nm and 541 nm. In contrast, Cell 5 exhibits a green Gaussian maximum at 560 nm, which is closer to the yellow Gaussian maxima in the other cells, which range between 557 nm and 588 nm. Moreover, the yellow Gaussian in Cell 5 is notably redshifted to 632 nm, further distinguishing it from the yellow Gaussian peaks observed in the other cells.

By comparing the fitted maxima of green fluorescence with the values obtained for β-carotene in section 6.2, an intriguing pattern emerges. Cells 1, 2, and especially 3 exhibit a noticeable blueshift relative to the reference values. In contrast, the green fluorescence in Cell 4 matches closely with the values for solvents characterized by lower refractive indices. Conversely, the green fluorescence of Cell 6 aligns more closely with the values for solvents with higher refractive indices.

FLIM of *R. glutinis* in the green region is depicted in Fig. 6.13. From the structure, it seems that the green fluorescence of interest is overwhelmed by the strong yellow fluorescence background, also observed in Fig. 6.10b. In this image, as well as in spectral maps at 532 nm and 442 nm (Figs. 6.11 and 6.12), the fluorescence comes from globule structures. In the FLIM image (Fig. 6.13), these structures appear as dark spots, and the fluorescence covers the rest of the cell. Another indication that it is not the green fluorescence supposedly coming from carotenoids is the lifetime value of 2.2 - 4 ns, which is an order of magnitude longer than the measured value in *Vischeria* sp. (0 - 706 ps) from Fig. 6.9 and in *H. pluvialis* (108 - 407 ps) from Fig. 6.19.

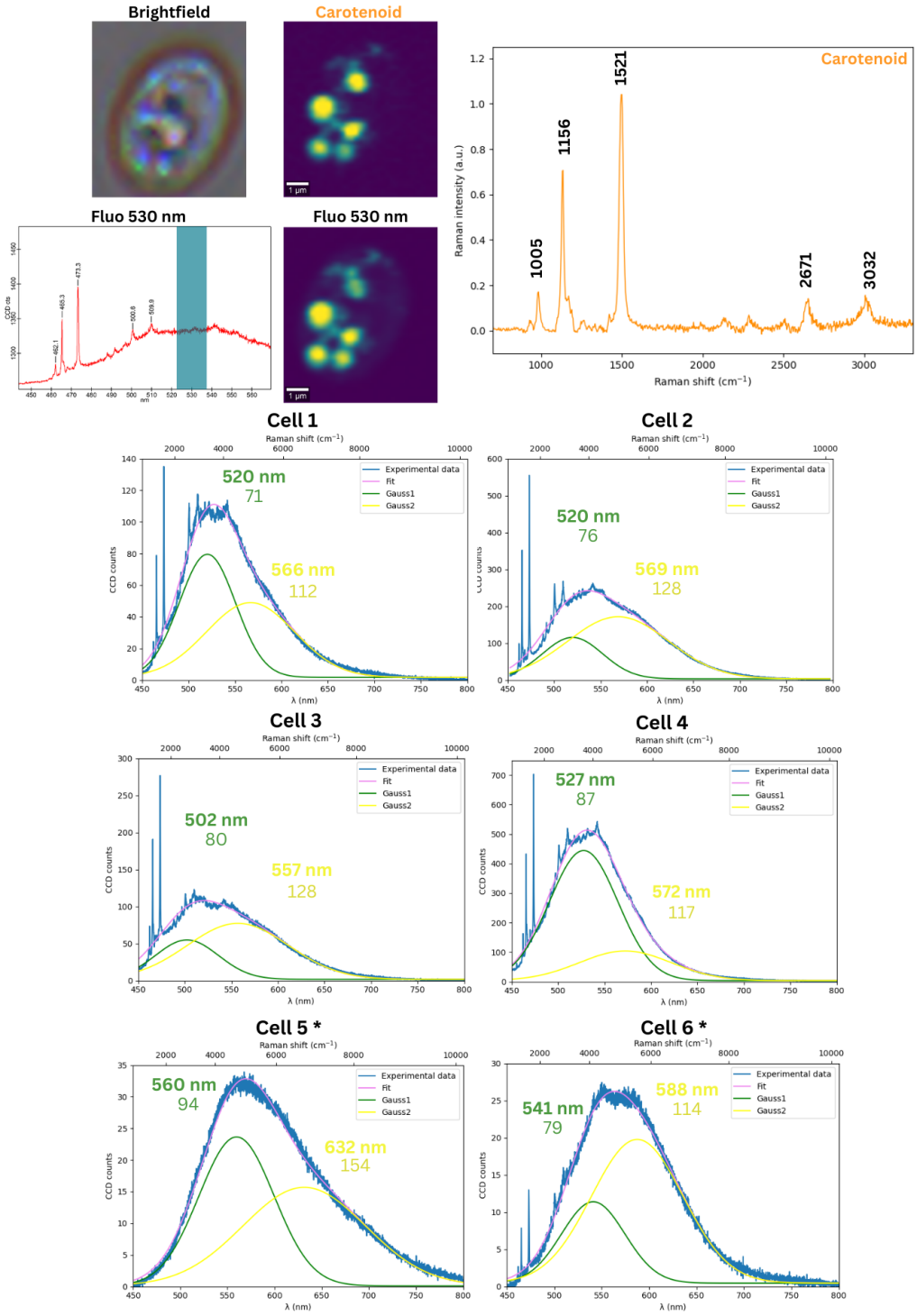


Figure 6.12: Spectral maps and spectra of *R. glutinis* obtained with blue excitation (442 nm) and a power of 50 µW, except for spectra marked with *, where 10 µW was used. The maps highlight the distribution of carotenoids and fluorescence across the cell. Spectral stitching spectra from several cells are also shown. The spectra were fitted using the sum of two Gaussians. The position of these Gaussians and the full width at half maximum (FWHM) are written in each graph.

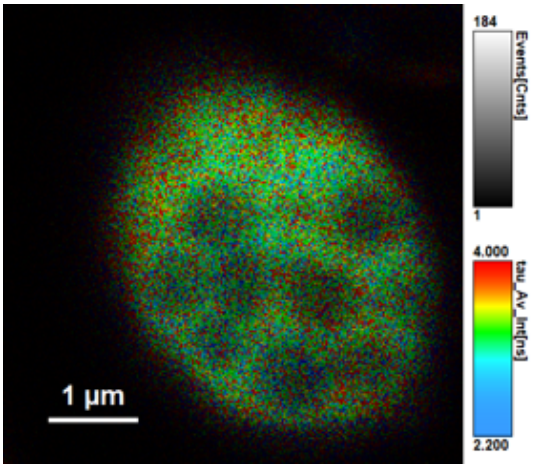


Figure 6.13: Fluorescence lifetime imaging (FLIM) of *R. glutinis*.

### 6.3.3 *Haematococcus pluvialis*

*Haematococcus pluvialis* was imaged using a widefield fluorescence microscope under blue excitation (Fig. 6.14). Fig. 6.14a illustrates the earlier green macrozoid stage of *H. pluvialis*, with flagella marked by a black arrow. The white arrow highlights the pyrenoid, a sub-cellular compartment within many algal chloroplasts that primarily serves as a center for carbon dioxide fixation, where RuBisCO (Ribulose-1,5-bisphosphate carboxylase/oxygenase) accumulates Kawano [2014]. In Fig. 6.14b, the same cell under blue excitation emits red fluorescence from chlorophyll.

Fig. 6.14c presents a mature cyst (aplanospore), which exhibits a bright red color due to the accumulation of astaxanthin within lipid droplets in the cells Niizawa et al. [2021]. In Fig. 6.14d, these cells are imaged under blue excitation. As the cells accumulate astaxanthin, the fluorescence predominantly shifts to the green-yellow region, with some residual red fluorescence from chlorophyll still present.

Spectral maps and spectra of the green stage of *H. pluvialis*, obtained with green excitation (532 nm), are shown in Fig. 6.15. Two laser powers were employed: 5 µW to detect carotenoids and fluorescence while avoiding bleaching and a higher power of 32 mW to detect other compounds with lower signals than carotenoids.

The chemical map of carotenoids at low power (5 µW) aligns with the red spot in the middle of the cell in brightfield. The distribution of fluorescence at 590 nm mirrors the carotenoid map, indicating a colocalization between carotenoid distribution and increased fluorescence background under green excitation. Additionally, the map showing fluorescence at 662 nm illustrates the distribution of chlorophyll fluorescence. The carotenoid spectrum reveals the most intensive vibration, $\nu_1$, at 1519 cm$^{-1}$, followed by $\nu_2$ at 1157 cm$^{-1}$ and $\nu_3$ at 1005 cm$^{-1}$. Two other weak vibrations are observed between $\nu_2$ and $\nu_1$ at 1193 cm$^{-1}$ and 1276 cm$^{-1}$. A combination vibration, $\nu_1$+$\nu_2$, is observed at 2668 cm$^{-1}$. The position of $\nu_1$ is slightly shifted to a lower wavenumber compared to the value 1523 cm$^{-1}$ measured for astaxanthin standard in most of the different solvents in section 6.2.2.

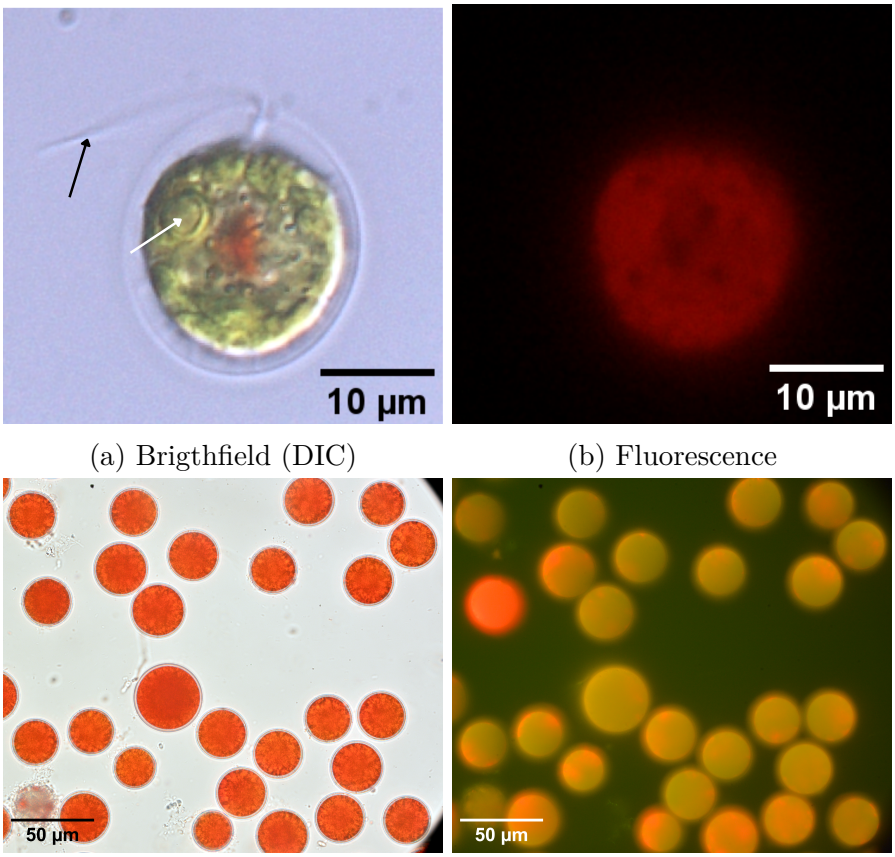


(a) Brigthfield (DIC) (b) Fluorescence

(c) Brightfield (d) Fluorescence

Figure 6.14: *H. pluvialis* imaged with a widefield fluorescence microscope in brightfield (a,c) and fluorescence contrast with blue excitation (b,d). (a,b) Green flagellated cell (black arrow) with pyrenoid (white arrow). (c,d) Mature cyst (aplanospore).

Liu and Huang [2016] reported the positions of astaxanthin vibrations as $\nu_1$ at 1516 $cm^{-1}$, $\nu_2$ at 1157 $cm^{-1}$, and $\nu_3$ at 1007 $cm^{-1}$. These values are comparable with our measured carotenoid spectra. Timlin et al. [2017] provided resonance Raman spectra for six common carotenoids found in photosynthetic organisms, including astaxanthin, and suggested that the position of $\nu_1$ can be used to distinguish between carotenoids. According to their data, our measured spectrum corresponds to β-carotene, for which Timlin et al. [2017] reported $\nu_1$ at 1519 $cm^{-1}$. The reported position of astaxanthin $\nu_1$ is the same as reported by Liu and Huang [2016] 1516 $cm^{-1}$. However, due to the microscope's spectral resolution, distinctions between astaxanthin and β-carotene can be challenging. Shao et al. [2019] provided additional Raman spectra data for astaxanthin, noting slightly higher frequencies for all three vibrations: $\nu_1 = 1520$ $cm^{-1}$, $\nu_2 = 1159$ $cm^{-1}$, and $\nu_3 = 1009$ $cm^{-1}$. Moreover, Ranga et al. [2009] identified that astaxanthin esters constitute over 80 % of the carotenoid content in *H. pluvialis*, confirming that our measured spectra are predominantly attributed to astaxanthin. To differentiate other carotenoids in *H. pluvialis*, advanced analytical techniques such as multivariate curve resolution, as demonstrated by Timlin et al. [2017] and Liu and Huang [2016], would be necessary.

At higher power (32 mW), additional components become apparent. The red

spectrum indicates starch, which accumulates around two pyrenoids in the cell. Similar to *Vischeria* sp, *H. pluvialis* also contains guanine crystals, as depicted in the guanine chemical map. The lipid spectrum features a peak at 3011 $cm^{-1}$, suggesting unsaturation. Another unsaturation marker at 1650 $cm^{-1}$ overlaps with a peak around 1586 $cm^{-1}$, which is the same peak as in *Vischeria* sp., probably assigned to retinoids. This peak will be further examined in the spectral maps of aplanospore (Fig. 6.16). The lipid chemical map shows that lipids are centrally located, corresponding to the red spot in the brightfield image and the carotenoid map, indicating that astaxanthin is contained within lipid droplets. The final component, referred to as Component 1, was not assigned, but peaks at 1450 $cm^{-1}$ and 1553 $cm^{-1}$ may suggest a different type of lipid. The Component 1 chemical map shows it occupying almost the entire cell. This component shows a good spatial correlation with the chlorophyll fluorescence map (see Fig. 6.15, Fluo 665). It could spectrally correspond to the thylakoid membrane of plastids and the proteins contained therein.

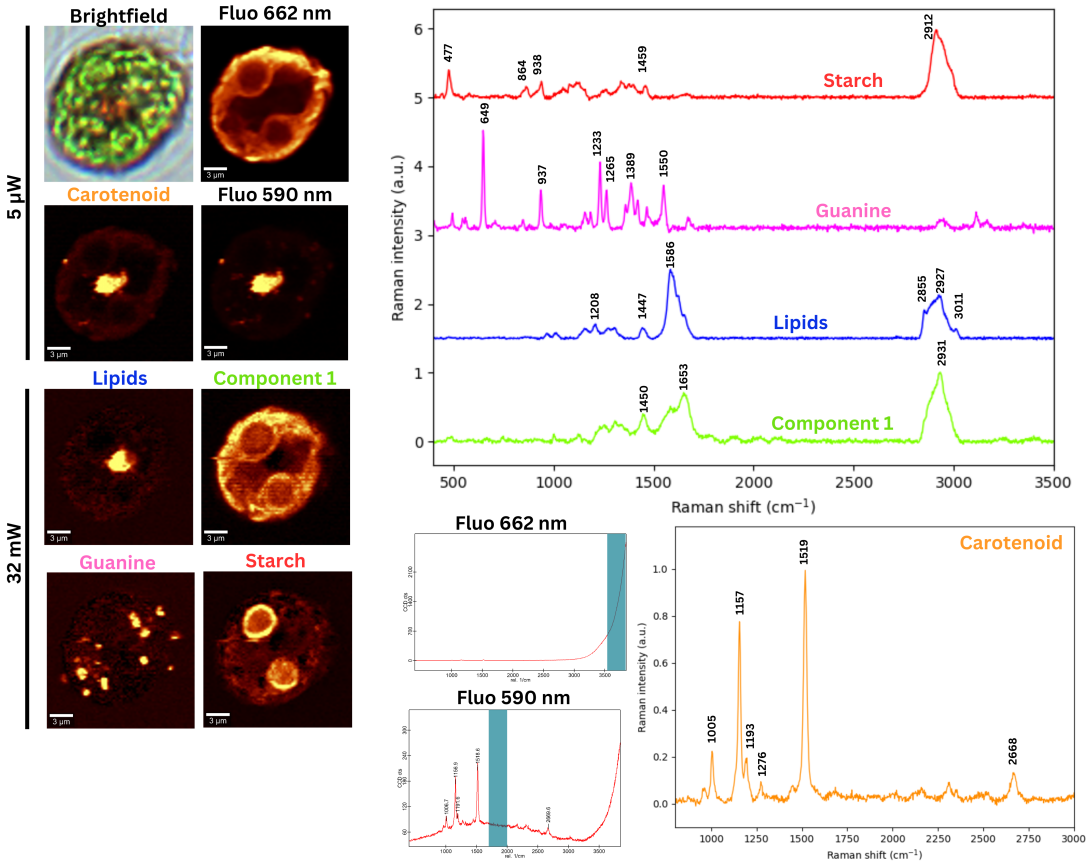


Figure 6.15: Spectral maps and spectra of the green stage of *H. pluvialis* obtained with green excitation (532 nm) at two laser powers: 5 µW and 32 mW.

Spectral maps and spectra of the cyst stage of *H. pluvialis* obtained with green excitation (532 nm) are depicted in Fig. 6.16. The carotenoid map at low power shows the most intense signal on the cell surface. This is likely due to two factors. Firstly, Ota et al. [2018] demonstrated that *H. pluvialis* cells, which store astaxanthin centrally (green-red cyst cells), rapidly react to intense light by redistributing astaxanthin to the cell periphery within 10 minutes of

exposure. Similar effects may occur in red cysts. The second, more significant, reason is reabsorption. The red cell is optically dense, causing both excitation and emission signals to be absorbed, even in the green region, where this is usually less problematic for carotenoids compared to blue [Lu et al., 2018]. Astaxanthin's absorption is red-shifted compared to β-carotene, and excitation at 532 nm is close to its absorption maximum at 492 nm in dimethyl sulfoxide [Buchwald and Jencks, 1968]. Also, here, the correlation between increased background around 590 in 5 μW spectrum and carotenoid distribution is observed. However, the above-mentioned effects count also for the fluorescence map. The carotenoid spectrum is the same as in the green stage in Fig. 6.15.

Even though the cell looks red, still some chlorophyll is left, as observed in the fluorescence around 662 nm map (Fluo 662 nm in Fig. 6.16), showing an increased background in the region of chlorophyll fluorescence.

At higher power, residual carotenoid is still observed. In this cell, it was possible to demix the lipids from the component with an intense peak at 1578 $cm^{-1}$, referred to as Component 2. The lipid spectrum belongs to unsaturated fatty acids, as it exhibits intense vibration at 1656 $cm^{-1}$, which is assigned to C=C stretching Wu et al. [2011]. The =C—H cis stretch at 1266 $cm^{-1}$ and the =C—H stretch at 3012 $cm^{-1}$ are also present. By applying eq. 6.1 to the intensity ratio of the 1656 and 1450 $cm^{-1}$ bands, a value of 2.69 is obtained, indicating a mixture of fatty acids with two and three double bonds. When compared to the Raman spectra of fatty acid standards reported by Wu et al. [2011], linoleic and linolenic acids with two and three double bonds, respectively, have similar shapes of the spectrum. At the chemical map of lipids, it is observed that the lipid bodies seem to fuse together in the upper part of the cell, possibly due to the absorption and higher laser power.

The stigma spectrum has a periodic toothed appearance due to the optical etaloning in the CCD detector, which is accentuated after subtracting the high fluorescence background shown in Fig. 6.16 in the Fluo 590 nm spectrum measured with 32 mW. Similar to the reddish globule in *Vischeria* sp., stigma can be identified not only by the Raman spectrum but also by the increased background around 590 nm in the Fluo 590 nm map (32 mW). It is evident that excitation light only reaches the cell center after carotenoids bleach, as stigma fluorescence was not observed at low power.

Component 2 exhibits its most intense vibrational mode at 1578 $cm^{-1}$, accompanied by several weaker modes at 1521 $cm^{-1}$, 1206 $cm^{-1}$, 1157 $cm^{-1}$, and 1009 $cm^{-1}$. Notably, a prominent vibrational feature between 1572 and 1596 $cm^{-1}$ is characteristic of Raman spectra of retinoids [Essendoubi et al., 2021, Kochan et al., 2015]. In Fig. 6.17, the spectrum of Component 2 is compared to the Raman spectrum of crystalline retinoic acid, revealing several similarities. Beyond the pronounced vibration at 1578 $cm^{-1}$, both spectra exhibit similarities around 1200 $cm^{-1}$, with the vibration at 1157 $cm^{-1}$ in Component 2 aligning precisely with that in retinoic acid. However, the peak at 1206 $cm^{-1}$ is slightly shifted towards lower wavenumbers in retinoic acid. Additionally, both spectra show a vibration at 1009 $cm^{-1}$.

Despite these similarities, the spectrum of Component 2 likely does not correspond exactly to retinoic acid, as indicated by the slight shift in the most intense vibration and the differing peak ratios around 1200 $cm^{-1}$. Kochan et al. [2015]

reported spectra of pure retinoic acid, retinal, and retinol, with band positions presented alongside those of retinol from Essendoubi et al. [2021] in Table 6.6. Among the retinoids listed in Table 6.6, retinoic acid most closely matches Component 2 in terms of the position of the most intense vibration and the alignment of the peak at 1206 $cm^{-1}$. Conversely, the position of the vibration at 1157 $cm^{-1}$ aligns best with retinol as measured by Essendoubi et al. [2021]. Regarding the shape and ratio of the peaks around 1200 $cm^{-1}$, retinal would be the best fit when compared to the spectra reported by Kochan et al. [2015].

To definitively assign Component 2's spectrum to a specific retinoid, a less noisy spectrum is needed, as weaker vibrations are currently obscured by noise. Additionally, other retinoids beyond those listed in Table 6.6 should be considered. Notably, Component 2's spectrum includes a peak at 1521 $cm^{-1}$, which is not observed in retinoids and may represent a residual unmixed carotenoid.

Comparing the distribution of lipids and Component 2 reveals colocalization. In the spectra of green *H. pluvialis* in Fig. 6.15, it was impossible to separate these two components due to their colocalization, suggesting that the retinol in *H. pluvialis* is likely localized within lipid droplets. This colocalization was also observed in *Vischeria* sp.. These findings align well with the works of Kochan et al. [2015] and Galler et al. [2016], where retinol was similarly observed in lipid droplets in mouse liver. The presence of retinoids in *H. pluvialis* and *Vischeria* sp. is reasonable, as retinoids are oxidative degradation products of carotenes and xanthophylls [Mordi et al., 2020].

Chemical maps of cyst cells measured with blue excitation (442 nm) are depicted in Fig. 6.18. The carotenoid spectrum is similar to that under green excitation, with an additional overtone vibration, $2\times\nu_1$, at 3038 $cm^{-1}$. The distribution of carotenoid and fluorescence at 530 nm is again similar, with the highest intensity at the cell periphery. This is likely due to reabsorption, which is even stronger with blue excitation. Additionally, some chlorophyll residues are observed in the distribution of fluorescence detected at around 680 nm (Fluo 680 map).

Table 6.6: Reported Raman band positions for retinol, retinal, and retinoic acid. One asterisk (*) indicates values from Kochan et al. [2015] and two asterisks (**) from Essendoubi et al. [2021].

| Band position ($cm^{-1}$) | | | |
|---|---|---|---|
| Retinol* | Retinol** | Retinal* | Retinoic acid* |
| 1594 | 1591 | 1572 | 1576 |
| 1275 | 1274 | 1280 | 1273 |
| 1201 | 1196 | 1201 | 1204 |
| 1163 | 1158 | 1168 | 1165 |
| 1014 | 1011 | 1011 | 1019 |

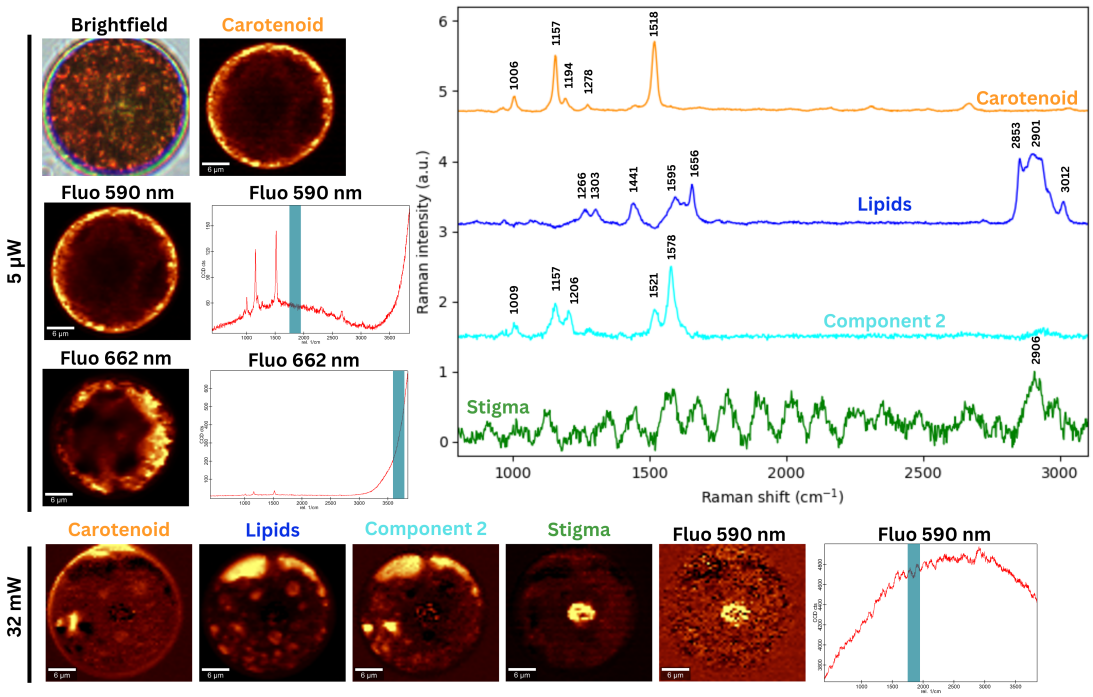


Figure 6.16: Spectral maps and spectra of cyst stage of *H. pluvialis* obtained with green excitation (532 nm) at two laser powers: 5 µW and 32 mW.

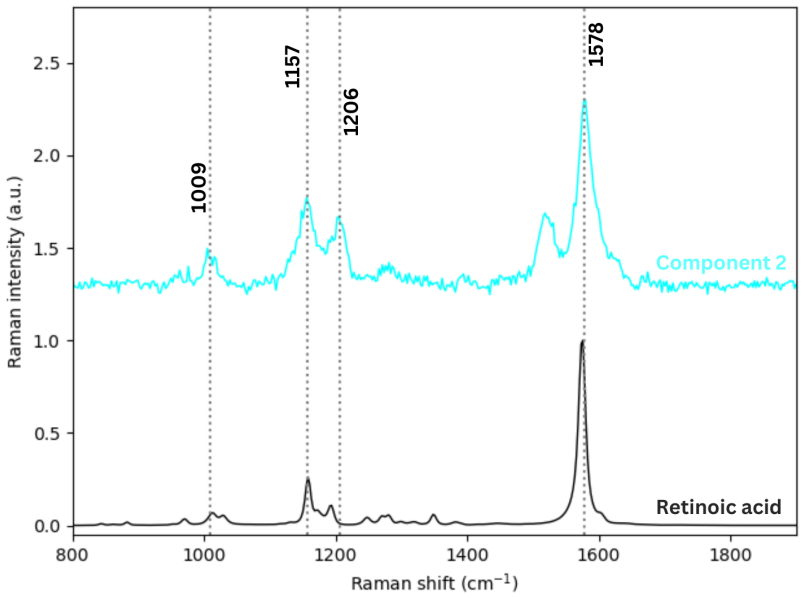


Figure 6.17: Spectrum of Component 2 from Raman mapping of aplanospore in Fig. 6.16 under green excitation (532 nm) compared to Raman spectrum of crystal of pure retinoic acid.

Fig. 6.18 also shows spectral stitching spectra from three different cells and different places indicated as a,b, and c. All spectra show a peak with a maximum ranging from 572 nm to 580 nm with FWHM around 90 nm, which is responsible for the yellow-green fluorescence observed in Fig. 6.14. The maximum of this peak is the same as the fluorescence maximum of astaxanthin in THF 574 nm

presented in section 6.2.2, indicating that this fluorescence likely originates from astaxanthin. Another intense peak is narrow fluorescence with FWHM around 19 nm at 682 nm. This peak corresponds to chlorophyll. All spectra show another broad fluorescence background with a position between 653 nm and 699 nm.

Figure 6.19 illustrates the FLIM of *H. pluvialis* red cyst cells using green region filters. As observed in the distribution of carotenoid Raman signals in the green (Fig. 6.16) and blue (Fig. 6.18) excitation, the FLIM signal is predominantly located at the cell periphery. The observed lifetimes range from 108 ps to 407 ps, comparable to those found in *Vischeria* sp. and works of Solovchenko et al. [2024] and Grudzinski et al. [2018] discussed above.

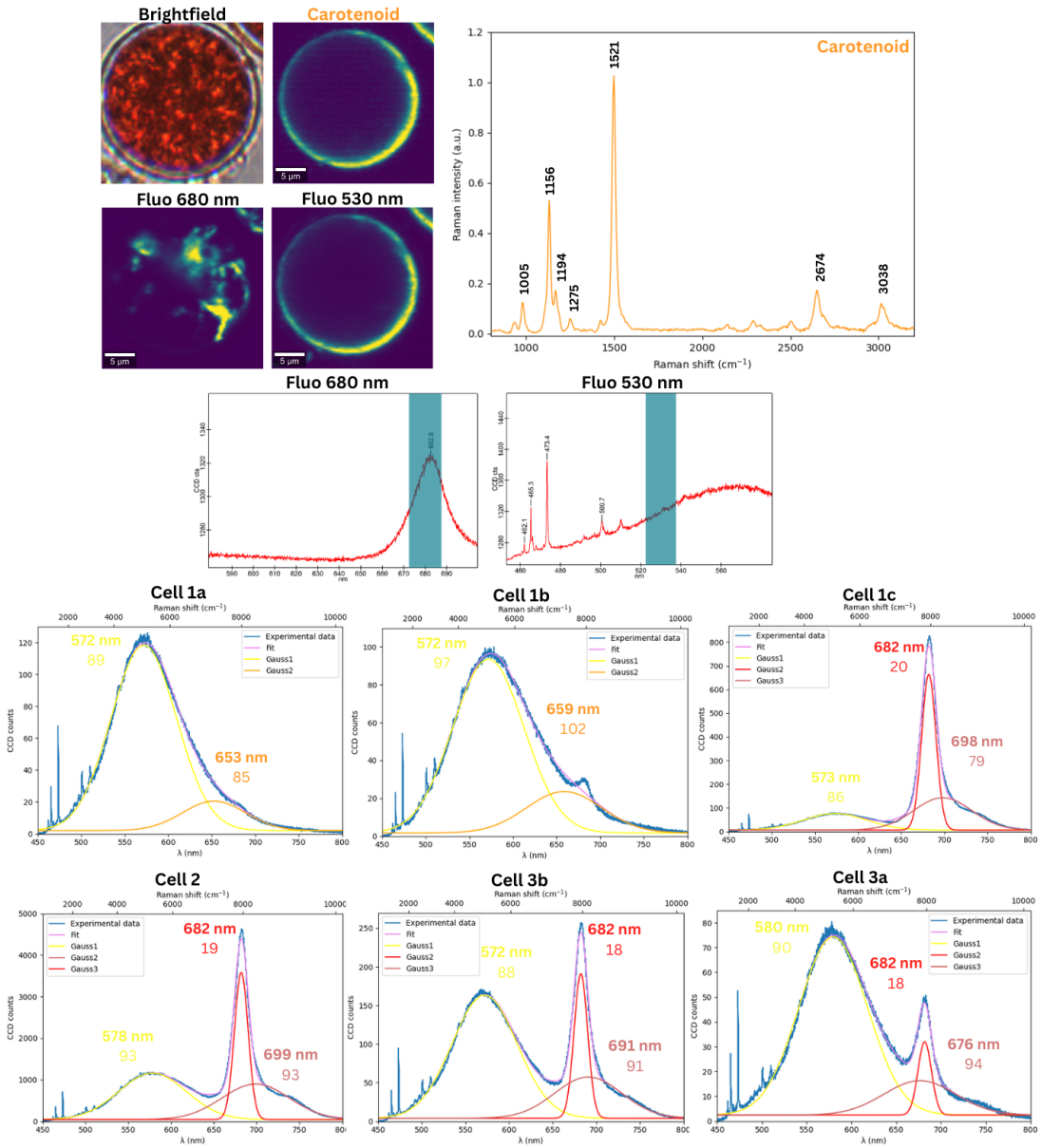


Figure 6.18: Spectral maps and spectra of cyst stage of *Haematococcus pluvialis* obtained with blue excitation (442 nm) and a power of 10 µW. The maps highlight the distribution of carotenoids and fluorescence across the cell. Spectral stitching spectra from several cells and places are also shown. The spectra were fitted using the sum of two or three Gaussians. The position of these Gaussians and the full width at half maximum (FWHM) are written in the graphs.

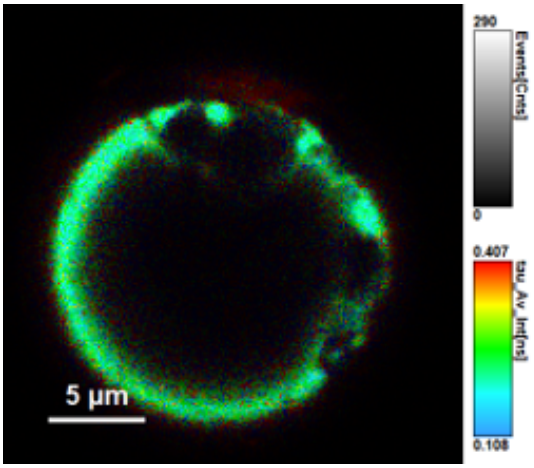


Figure 6.19: Fluorescence lifetime imaging (FLIM) of *H. pluvialis* red cyst cell.

# Conclusion

This diploma thesis dealt with the study of the spectroscopic properties of two model carotenoids, β-carotene and astaxanthin, in various solvents and directly in microorganisms that contain these carotenoids as part of their photosynthetic system or as antioxidants and substances protecting them against the detrimental effect of excessive light. The basic method was confocal Raman microscopy used in a manner that allowed simultaneous detection of Raman scattering and confocally detected fluorescence emission. These measurements were complemented by measurements of absorption spectra of carotenoid solutions and fluorescence-lifetime imaging microscopy (FLIM) of selected microorganisms. The scope and design of the experiments, however, was limited by the capabilities of the available apparatus.

The objective of this work was to determine whether carotenoids are responsible for the still not fully understood green autofluorescence (GAF) observed in various organisms, which has been repeatedly associated with the presence of carotenoids by various authors. With this aim, selected organisms were examined, namely *Haematococcus pluvialis*, *Vischeria* sp., and *Rhodotorulla glutinis*.

Our study found that solutions of both β-carotene and astaxanthin in various solvents exhibit weak fluorescence under blue excitation (falling within their electronic absorption band), with emission maxima in the green to yellow region of the visible spectrum. For β-carotene, the broad emission band maximum ranged from 524 nm to 545 nm, while astaxanthin's emission maximum was shifted to the green-yellow to yellow region, ranging from 556 nm to 574 nm. Both carotenoids exhibited a bathochromic shift in solvents with higher refractive indices (THF, mineral oil, TCM), suggesting that their emission spectra in biological structures could depend on their surroundings.

Furthermore, our study indicated that the absorption of β-carotene generally correlates with its solubility in different solvents rather than with the magnitude of its absorption coefficients for the respective solvents. This suggests that its spectroscopic properties (including fluorescence) in biological structures can be strongly influenced by the aggregation state or the properties of the environment. This is another reason for caution when transferring conclusions obtained from solution measurements to biological structures. For instance, the fluorescence intensity of β-carotene in hexane reached its maximum at concentrations almost six times lower than its reported solubility.

Analysis of the Raman spectra of both carotenoids in different solvents revealed minimal sensitivity of their vibrational spectra to the environment. Our measurements supported this paradoxical fact, reported in the literature by other authors. The Raman band corresponding to the $\nu_1$ vibration of β-carotene in solvents with higher refractive indices showed only a slight down-shift (2-3 $cm^{-1}$), while the position of this band in astaxanthin remained consistent across all solvents used. The conclusion from our solution measurements was that the Raman spectra of the investigated carotenoids likely reveal very little about their immediate surroundings.

From this perspective, a rather surprising finding emerged from *in vivo* measurements of Raman maps of *Vischeria* sp. cells, where we reliably identified

three types of Raman spectra of the carotenoids present. It should be noted that these different Raman spectra were obtained using 532 nm excitation, i.e., in the green spectral region, and that two of these spectra were observed using extremely low excitation power. It must be emphasized that these two different spectra were extracted from the same Raman maps, so the observed spectral difference is unquestionable. One spectrum obtained using extremely low power on living cells before photobleaching was co-localized with the plastid, while the other was co-localized with the reddish globule. The spectra showed significant differences in the position of the $\nu_1$ band and the intensity ratio of the $\nu_1$ and $\nu_2$ bands. A third carotenoid Raman spectrum was detected upon higher power excitation. This spectrum was likely co-localized with larger lipid droplets, where carotenoids, due to the hydrophobic environment, should be better protected from photobleaching via singlet oxygen and ROS. The observation of three different Raman spectra of carotenoids may seem incompatible with the idea of a single carotenoid being present in three different environments. Rather, it suggests the presence of three different carotenoids. Using blue excitation (442 nm), which allowed the simultaneous detection of the resonance Raman spectrum and fluorescence emission, only a single carotenoid spectrum similar to the non-resonant Raman spectrum obtained from plastids using green excitation (532 nm) was observed, while the carotenoid in the reddish globule was virtually undetectable, probably due to reabsorption or photodestruction.

In the case of *in vivo* measurements on *R. glutinis* cells, different Raman spectra of carotenoids were also observed under different excitations. The differences in the spectra obtained under different excitations could be explained by the presence of different carotenoids with different absorption spectra and benefiting from different resonance enhancement. Based on spectral similarity to published Raman spectra, the spectrum obtained under green excitation (532 nm) would correspond to the carotenoid torulene, which exhibits a red-shifted absorption maximum compared to β-carotene, whose spectrum was probably observed under blue excitation (442 nm). Both carotenoids were likely located in the same lipid droplets. In *H. pluvialis*, only one carotenoid spectrum attributable to astaxanthin was observed in the whole cell.

The results from microorganisms demonstrate that Raman mapping, combined with proper spectral decomposition, can be used to identify and localize different carotenoids in different cell organelles. At the same time, it highlights the possibility of incorrect interpretation and the problematic transfer of conclusions obtained using different excitation wavelengths. This issue deserves more detailed study, especially since most published works dealing with carotenoids at the single-cell level either ignore or do not discuss these differences.

Simultaneous *in vivo* measurements of Raman scattering and fluorescence emission of the cells using blue excitation (442 nm) revealed a very good agreement between the chemical map of carotenoid occurrence and the fluorescence map of green emission at around 530 - 550 nm. This suggests that carotenoids present in some cellular structures could indeed be a source of enigmatic GAF. Moreover, in the case of *R. glutinis* and *H. pluvialis*, a particular correlation was observed between the distribution of carotenoids deduced from the non-resonant Raman spectrum obtained under green excitation (532 nm) and the increased background in the yellow region at around 590 nm. It should be noted that the

excitation of 532 nm is already outside the absorption band of carotenoids, however, it reaches its beginning and can still be slightly absorbed by carotenoids, contributing to the increased background of the Raman spectrum. However, it cannot be ruled out that this very weak yellow emission originates from a fluorophore other than carotenoids.

Furthermore, supporting the hypothesis that carotenoids are the source of the enigmatic green fluorescence, it should be mentioned that the positions of the fluorescence maxima fitted by Gaussian curves for the green region in *Vischeria* sp. are in good agreement with β-carotene fluorescence maxima in solvents with higher refractive indices. Similarly, for *H. pluvialis*, these values are consistent with the measured fluorescence of astaxanthin in THF. In the case of *R. glutinis*, the green autofluorescence is slightly blue-shifted compared to the fluorescence of carotenoids in solvents.

Finally, although the lifetimes determined in this work by *in vivo* FLIM in the cells of *Vischeria* sp. and *H. pluvialis* are very short, they are comparable to the values reported by other authors for the green autofluorescence of other cells or biological objects containing carotenoids.

Despite many indications that the source of GAF is indeed carotenoids, this work cannot exclude the presence of other fluorescent compounds co-localizing with carotenoids, such as some metabolites or degradation products like retinoids, which we have detected based on their Raman spectra in the cells of *Vischeria* sp. and *H. pluvialis*. More experiments will be needed to fully demonstrate that carotenoids are the source of the green autofluorescence. We hope that the results presented in this thesis will be valuable to anyone who will further investigate this fascinating issue.

# Bibliography


Avantar mineral oil, liquid — vwr. https://nl.vwr.com/store/product/20268800/mineral-oil-heavy-white-oil. Accessed: 2024-07-01.

OLYMPUS Confocal confocal microscopy - introduction — olympus ls. https://www.olympus-lifescience.com/en/microscope-resource/primer/techniques/confocal/confocalintro/. Accessed: 2024-07-01.

Edinburgh Instruments Raman what is raman spectroscopy? — raman spectroscopy principle. https://www.edinst.com/de/blog/what-is-raman-spectroscopy/. Accessed: 2024-07-01.

Edinburgh Instruments microscope confocal raman microscopy — confocal microscope. https://www.edinst.com/blog/what-is-confocal-raman-microscopy/. Accessed: 2024-07-01.

Oxford instruments— optical etaloning in charge coupled devices. https://andor.oxinst.com/learning/view/article/optical-etaloning-in-charge-coupled-devices. Accessed: 2024-07-15.

OLYMPUS Fluorescence fluorescence microscopy - basic concepts in fluorescence — olympus ls. https://www.olympus-lifescience.com/en/microscope-resource/primer/techniques/fluorescence/fluorescenceintro/, a. Accessed: 2024-07-01.

OLYMPUS Widefield introduction to fluorescence microscopy — nikon's microscopyu. https://www.microscopyu.com/techniques/fluorescence/introduction-to-fluorescence-microscopy, b. Accessed: 2024-07-01.

Sigma-Aldrich laboratory basics: Refractive index. https://www.sigmaaldrich.com/deepweb/assets/sigmaaldrich/marketing/global/documents/614/456/labbasics_pg144.pdf, a. Accessed: 2024-07-01.

Yeast peptone dextrose broth. https://www.sigmaaldrich.com/CZ/en/product/sigma/y1375, b. Accessed: 2024-07-14.

Microbe Onlinel fluorescence microscope: Principle, types, applications • microbe online. https://microbeonline.com/fluorescence-microscope-principle-types-applications/. Accessed: 2024-07-01.

P. Abdi and M. Atighehchian. *Principles of In Vivo Confocal Microscopy*, pages 1–12. Springer London, London, 2022. doi: 10.1007/978-1-4471-7517-9_1.

L. Adler, N. P. Boyer, Ch. Chen, Z. Ablonczy, R. K. Crouch, and Y. Koutalos. *The 11-cis Retinal Origins of Lipofuscin in the Retina*, volume 134, chapter 31. Elsevier, Charleston, South Carolina, USA, 2015.

H. W. Bischoff and H. Ch. Bold. *Some soil algae from Enchanted Rock and related algal species*, volume IV. of *Phycological studies*. University of Texas Publication, Austin, Texas, 1963.

D. H. Blankenhorn and H. Braunstein. Carotenoids in man. III. microscopic pattern of fluorescence in atheromas, and its relation to their growth. *Journal of Clinical Investigation*, 37(2):160–165, 1958. doi: 10.1172/jci103594.

S. L. Bondarev and V. N. Knyukshto. Fluorescence from the S1(2 1Ag) state of all-trans-β-carotene. *Chemical Physics Letters*, 225(4):346–350, 1994. doi: 10.1016/0009-2614(94)87092-6.

N. K. Bozalan and F. Karadeniz. Carotenoid profile, total phenolic content, and antioxidant activity of carrots. *International Journal of Food Properties*, 14: 1060–1068, 2011. doi: 10.1080/10942910903580918.

M. Buchwald and W. P. Jencks. Optical properties of astaxanthin solutions and aggregates. *Biochemistry*, 7(2):834–843, 1968. doi: 10.1021/bi00842a042.

P. Buzzini, M. Innocenti, B. Turchetti, D. Libkind, M. van Broock, and N. Mulinacci. Carotenoid profiles of yeasts belonging to the genera *Rhodotorula, Rhodosporidium, Sporobolomyces*, and *Sporidiobolus*. *Canadian Journal of Microbiology*, 53(8):1024–1031, 2007. doi: 10.1139/w07-068.

M. T. C. Campos, L. F. Maia, H. F. Dos Santos, H. G. M. Edwards, and L. F. C. de Oliveira. Revealing the chemical synergism in coloring tomatoes by Raman spectroscopy. *Journal of Raman Spectroscopy*, 54(11):1314–1326, 2023. doi: 10.1002/jrs.6471.

R. C. Chisté, M. Freitas, A. Z. Mercadante, and E. Fernandes. Carotenoids inhibit lipid peroxidation and hemoglobin oxidation, but not the depletion of glutathione induced by ROS in human erythrocytes. *Life Sciences*, 99(1-2): 52–60, 2014. doi: 10.1016/j.lfs.2014.01.059.

N. E. Craft and J. H. Soares. Relative solubility, stability, and absorptivity of lutein and β-carotene in organic solvents. *Journal of Agricultural and Food Chemistry*, 40(3):431–434, 1992. doi: 10.1021/jf00015a013.

A. C. Croce and G. Bottiroli. Autofluorescence spectroscopy and imaging: A tool for biomedical research and diagnosis. *European Journal of Histochemistry: EJH*, 58:320–337, 10 2014. doi: 10.4081/EJH.2014.2461.

E. F. Călin, S. I. P. Popescu, C. C. C. Cernat, C. Patoni, M. Popescu, and O. Mușat. Lipofuscin: a key compound in ophthalmic practice. *Romanian Journal of Ophthalmology*, 65:109, 6 2021. doi: 10.22336/RJO.2021.23.

T. Dieing, O. Hollricher, and J. Toporski. *Confocal Raman Microscopy*. Springer Series in Optical Sciences. Springer, Heidelberg, 2011. doi: doi:10.1007/978-3-642-12522-5.

L. Donaldson. Autofluorescence in plants. *Molecules*, 25(10):2393, 2020. doi: 10.3390/molecules25102393.

M. Eliáš, R. Amaral, K. P. Fawley, M. W. Fawley, Y. Němcová, J. Neustupa, P. Přibyl, L. M. A. Santos, and T. Ševčíková. *Eustigmatophyceae*, pages 367–406. Springer International Publishing, Cham, 2017. doi: 10.1007/978-3-319-28149-0_39.

M. Essendoubi, F. Alsamad, P. Noël, M. Meunier, A. Scandolera, J. Sandré, M. Manfait, C. Gobinet, R. Reynaud, and O. Piot. Combining Raman imaging and MCR-ALS analysis for monitoring retinol permeation in human skin. *Skin Research and Technology*, 27(6):1100–1109, 2021. doi: 10.1111/srt.13069.

L. Ettema, B. Lochocki, J. J. M. Hoozemans, J. F. de Boer, and F. Ariese. Label-free Raman and fluorescence imaging of amyloid plaques in human Alzheimer's disease brain tissue reveal carotenoid accumulations. *Journal of Optics*, 24(5): 12, 2022. doi: 10.1088/2040-8986/ac5b51.

J. Fiedor, M. Przetocki, A. Siniarski, G. Gajos, N. Spiridis, K. Freindl, and K. Burda. β.

L. S. Forster and R. Livingston. The absolute quantum yields of the fluorescence of chlorophyll solutions. *Journal of Chemical Physics*, 20(8):1315–1320, 1952. doi: 10.1063/1.1700727.

H. A. Frank and R. L. Christensen. *Excited Electronic States, Photochemistry and Photophysics of Carotenoids*, pages 167–188. Birkhäuser Basel, Basel, 2008. doi: 10.1007/978-3-7643-7499-0_9.

H. A. Frank, A. J. Young, G. Britton, and R. J. Cogdell. *The Photochemistry of Carotenoids*, volume 8 of *Advances in Photosynthesis*. Kluwer Academic Publishers, New York, Boston, Dordrecht, London, Moscow, 2004. doi: 10.1007/0-306-48209-6.

K. Galler, R. P. Requardt, U. Glaser, R. Markwart, T. Bocklitz, M. Bauer, J. Popp, and U. Neugebauer. Single cell analysis in native tissue: Quantification of the retinoid content of hepatic stellate cells. *Scientific Reports 2016 6:1*, 6:1–8, 2016. doi: 10.1038/srep24155.

T. Gillbro and R. J. Cogdell. Carotenoid fluorescence. *Chemical Physics Letters*, 158(3-4):312–316, 1989. doi: 10.1016/0009-2614(89)87342-7.

W. Grudzinski, M. Piet, R. Luchowski, E. Reszczynska, R. Welc, R. Paduch, and W. I. Gruszecki. Different molecular organization of two carotenoids, lutein and zeaxanthin, in human colon epithelial cells and colon adenocarcinoma cells. *Spectrochimica Acta Part A: Molecular and Biomolecular Spectroscopy*, 188: 57–63, 2018. doi: 10.1016/J.SAA.2017.06.041.

D. A. Hartzler, D. M. Niedzwiedzki, D. A. Bryant, R. E. Blankenship, Y. Pushkar, and S. Savikhin. Triplet excited state energies and phosphorescence spectra of (bacterio)chlorophylls. *Journal of Physical Chemistry B*, 118(26):7221–7232, 2014. doi: 10.1021/jp500539w.

H. Hashimoto, Ch. Uragami, and R. J. Cogdell. *Carotenoids and Photosynthesis*, pages 111–139. Springer International Publishing, Cham, 2016. doi: 10.1007/978-3-319-39126-7_4.

H. Hashimoto, C. Uragami, N. Yukihira, A. T. Gardiner, and R. J. Cogdell. Understanding/unravelling carotenoid excited singlet states. *Journal of the Royal Society Interface*, 15(141):15, 2018. doi: 10.1098/rsif.2018.0026.

N. M. Hassan, N. A. Yusof, A. F. Yahaya, N. N. M. Rozali, and Rashidi Othman. Carotenoids of capsicum fruits: Pigment profile and health-promoting functional attributes. *Antioxidants*, 8, 10 2019. doi: 10.3390/ANTIOX8100469.

M. Honda, T. Kodama, H. Kageyama, T. Hibino, Wahyudiono, H. Kanda, and M. Goto. Enhanced solubility and reduced crystallinity of carotenoids, β-carotene and astaxanthin, by Z-isomerization. *European Journal of Lipid Science and Technology*, 120(11):8, 2018. doi: 10.1002/ejlt.201800191.

H. Kawai. Green flagellar autofluorescence in brown algal swarmers and their phototactic responses. *Botanical Magazine, Tokyo*, 105:171–184, 1992. doi: 10.1007/BF02489413.

S. Kawano. *Chloroplasts*, pages 45–70. Springer Japan, Tokyo, 2014. ISBN 978-4-431-54941-3. doi: 10.1007/978-4-431-54941-3_3.

S. Khandelwal and R. K. Saxena. Age-dependent increase in green autofluorescence of blood erythrocytes. *Journal of Biosciences*, 32(6):1139–1145, 2007.

D. M. M. Kleinegris, M. A. van Es, M. Janssen, W. A. Brandenburg, and R. H. Wijffels. Carotenoid fluorescence in *Dunaliella salina*. *Journal of Applied Phycology*, 22(5):645–649, 2010. doi: 10.1007/s10811-010-9505-y.

K. Kochan, K. M. Marzec, E. Maslak, S. Chlopicki, and M. Baranska. Raman spectroscopic studies of vitamin A content in the liver: a biomarker of healthy liver. *Analyst*, 140:2074–2079, 2015. doi: 10.1039/C4AN01878H.

M. G. Lagorio, G. B. Cordon, and A. Iriel. Reviewing the relevance of fluorescence in biological systems. *Photochemical Photobiological Sciences*, 14(9):1538–1559, 2015. doi: 10.1039/c5pp00122f.

J.J. Lamb, G. Røkke, and M.F. Hohmann-Marriott. Chlorophyll fluorescence emission spectroscopy of oxygenic organisms at 77 k. *Photosynthetica*, 56:105–124, 2018. doi: 10.1007/s11099-018-0791-y.

T. Y. Li, Y. Zhang, N. Gong, Z. W. Li, C. L. Sun, and Z. W. Men. The chlorophyll a fluorescence modulated by all-trans-β-carotene in the process of photosystem II. *International Journal of Molecular Sciences*, 17(6):6, 2016. doi: 10.3390/ijms17060978.

J. H. Liu and Q. Huang. Screening of astaxanthin-hyperproducing *Haematococcus pluvialis* using fourier transform infrared (FT-IR) and Raman microspectroscopy. *Applied Spectroscopy*, 70(10):1639–1648, 2016. doi: 10.1177/0003702816645605.

M. J. Llansola-Portoles, A. A. Pascal, and B. Robert. Electronic and vibrational properties of carotenoids: from *in vitro* to *in vivo*. *Journal of the Royal Society Interface*, 14, 2017. doi: 10.1098/RSIF.2017.0504.

M. J. Llansola-Portoles, A. A. Pascal, and B. Robert. *Chapter Four - Resonance Raman: A powerful tool to interrogate carotenoids in biological matrices*, volume 674, pages 113–135. Academic Press, 2022. doi: https://doi.org/10.1016/bs.mie.2022.03.068.

D. A. Long. *The Raman Effect: A Unified Treatment of the Theory of Raman Scattering by Molecules*. John Wiley, Chichester, England, 2002. ISBN 978-0-471-49028-9.

L. Lu, L. Shi, J. Secor, and R. Alfano. Resonance Raman scattering of β-carotene solution excited by visible laser beams into second singlet state. *Journal of Photochemistry and Photobiology B: Biology*, 179:18–22, 2018. doi: 10.1016/j.jphotobiol.2017.12.022.

T. Maoka. Carotenoids as natural functional pigments. *Journal of Natural Medicines*, 74:1–16, 2020. doi: 10.1007/s11418-019-01364-x.

M. M. Mathews-Roth. Presence of carotenoids in the erythrocyte membranes of carotenemic and noncarotenemic individuals. *Clin Chem*, 21(2):258–9, 1975.

W. Miki. Biological functions and activities of animal carotenoids. *Pure and Applied Chemistry*, 63(1):141–146, 1991. doi: 10.1351/pac199163010141.

P. Mojzeš, L. Gao, T. Ismagulova, J. Pilátová, Š. Moudříková, O. Gorelova, A. Solovchenko, L. Nedbal, and A. Salih. Guanine, a high-capacity and rapid-turnover nitrogen reserve in microalgal cells. *Proceedings of the National Academy of Sciences of the United States of America*, 117(51):32722–32730, 2020. doi: 10.1073/pnas.2005460117.

C. R. Mordi, O. T. Ademosun, Ch. O. Ajanaku, I. O. Olanrewaju, and J. C. Walton. Free radical mediated oxidative degradation of carotenes and xanthophylls. *Molecules*, 25, 2020. doi: 10.3390/MOLECULES25051038.

A. C. Mot, M. Pârvu, A. E. Pârvu, O. Rosca-Casian, N. E. Dina, N. Leopold, R. Silaghi-Dumitrescu, and C. Mircea. Reversible naftifine-induced carotenoid depigmentation in *Rhodotorula mucilaginosa* (A. Jorg.) FC Harrison causing onychomycosis. *Scientific Reports*, 7:12, 2017. doi: 10.1038/s41598-017-11600-7.

T. Naz, S. Ullah, Y. Nazir, S. Q. Li, B. Iqbal, Q. Liu, H. Mohamed, and Y. D. Song. Industrially important fungal carotenoids: Advancements in biotechnological production and extraction. *Journal of Fungi*, 9(5):29, 2023. doi: 10.3390/jof9050578.

I. Niizawa, B. Y. Espinaco, S. E. Zorrilla, and G. A. Sihufe. *Astaxanthin production by autotrophic cultivation of Haematococcus pluvialis: A success story*, pages 71–89. Academic Press, 2021. doi: 10.1016/B978-0-12-823304-7.00005-2.

E. I. Nikelshparg, D. N. Bratashov, M. I. Nikelshparg, and V. V. Anikin. Fate of carotenoids in the closed living system of gall-gall wasp-parasitoid. *Chemoecology*, 32(1):31–40, 2022. doi: 10.1007/s00049-021-00364-2.

S. Ota, A. Morita, S. Ohnuki, A. Hirata, S. Sekida, K. Okuda, Y. Ohya, and S. Kawano. Carotenoid dynamics and lipid droplet containing astaxanthin in response to light in the green alga *Haematococcus pluvialis*. *Scientific Reports*, 8:10, 2018. doi: 10.1038/s41598-018-23854-w.

M. Z. Pacia, J. Pukalski, K. Turnau, M. Baranska, and A. Kaczor. Lipids, hemoproteins and carotenoids in alive *Rhodotorula mucilaginosa* cells under pesticide decomposition - Raman imaging study. *Chemosphere*, 164:1–6, 2016. doi: 10.1016/j.chemosphere.2016.08.069.

T. Polívka and V. Sundström. Ultrafast dynamics of carotenoid excited states -: From solution to natural and artificial systems. *Chemical Reviews*, 104(4): 2021–2071, 2004. doi: 10.1021/cr020674n.

C. V. Raman and K. S. Krishnan. A new type of secondary radiation. *Nature*, 121(3048):501–502, 1928. doi: 10.1038/121501c0.

R. Ranga, A. R. Sarada, V. Baskaran, and G. A. Ravishankar. Identification of carotenoids from green alga *Haematococcus pluvialis* by HPLC and LC-MS (APCI) and their antioxidant properties. *Journal of Microbiology and Biotechnology*, 19(11):1333–1341, 2009. doi: 10.4014/jmb.0905.03007.

B. Robert. *The Electronic Structure, Stereochemistry and Resonance Raman Spectroscopy of Carotenoids*, volume 8 of *Advances in Photosynthesis and Respiration*. Springer, Dordrecht, Dordrecht, 1999. doi: 10.1007/0-306-48209-6_10.

J. E. Sanger. Quantitative investigations of leaf pigments from their inception in buds through autumn coloration to decomposition in falling leaves. *Ecology*, 52:1075–1089, 11 1971. doi: 10.2307/1933816.

T. Schweizer, H. Kubach, and T. Koch. Investigations to characterize the interactions of light radiation, engine operating media and fluorescence tracers for the use of qualitative light-induced fluorescence in engine systems. *Automotive and Engine Technology*, 6(3):275–287, 2021. doi: 10.1007/s41104-021-00092-3.

Y. N. Shao, W. M. Gu, L. J. Jiang, and Y. M. Zhu. Study on the visualization of pigment in *Haematococcus pluvialis* by Raman spectroscopy technique. *Scientific Reports*, 9:9, 2019. doi: 10.1038/s41598-019-47208-2.

Y. She, X. Gao, X. Jing, J. Wang, Y. B. Dong, J. Z. Cui, H. D. Xue, Z. K. Li, and D. R. Zhu. Effects of nitrogen source and nacl stress on oil production in *Vischeria* sp. wl1 (*Eustigmatophyceae*) isolated from dryland biological soil crusts in china. *Journal of Applied Phycology*, 34(3):1281–1291, 2022. doi: 10.1007/s10811-022-02720-3.

A. Solovchenko, E. Lobakova, A. Semenov, O. Gorelova, T. Fedorenko, O. Chivkunova, E. Parshina, G. Maksimov, N. N. Sluchanko, and E. Maksimov. Multimodal non-invasive probing of stress-induced carotenogenesis in the cells of microalga *Bracteacoccus aggregatus*. *Protoplasma*, pages 1–21, 2024. doi: 10.1007/S00709-024-01956-9/FIGURES/11.

W. Stahl and H. Sies. Antioxidant activity of carotenoids. *Molecular Aspects of Medicine*, 24(6):345–351, 2003. doi: 10.1016/s0098-2997(03)00030-x.

W. Stahl and H. Sies. Carotenoids and flavonoids contribute to nutritional protection against skin damage from sunlight. *Molecular Biotechnology*, 37(1): 26–30, 2007. doi: 10.1007/s12033-007-0051-z.

W. Stahl and H. Sies. β-carotene and other carotenoids in protection from sunlight. *American Journal of Clinical Nutrition*, 96(5):1179S–1184S, 2012. doi: 10.3945/ajcn.112.034819.

M. Stoyneva-Gärtner, P. Stoykova, B. Uzunov, I. Dincheva, I. Atanassov, P. Draganova, C Borisova, and G. Gärtner. Carotenoids in five aeroterrestrial strains from *Vischeria/Eustigmatos* group: updating the pigment pattern of eustigmatophyceae. *Biotechnology and Biotechnological Equipment*, 33:250–267, 2019. doi: 10.1080/13102818.2018.1562984.

P. Swapnil, M. Meena, S. K. Singh, U. P. Dhuldhaj, Harish, and A. Marwal. Vital roles of carotenoids in plants and humans to deteriorate stress with its structure, biosynthesis, metabolic engineering and functional aspects. *Current Plant Biology*, 26:11, 2021. doi: 10.1016/j.cpb.2021.100203.

Y. Z. Tang and F. C. Dobbs. Green autofluorescence in dinoflagellates, diatoms, and other microalgae and its implications for vital staining and morphological studies. *Applied and Environmental Microbiology*, 73(7):2306–2313, 2007. doi: 10.1128/aem.01741-06.

J. A. Timlin, A. M. Collins, T. A. Beechem, M. Shumskaya, and E. T. Wurtzel. *Localizing and Quantifying Carotenoids in Intact Cells and Tissues*, page Ch. 03. InTech, Rijeka, 2017. doi: 10.5772/68101.

M. Trojak and E. Skowron. Improvement of plant heat tolerance by modification of xanthophyll cycle activity. *World Scientific News*, pages 51–70, 04 2017.

F. I. Tsuji. *Early History, Discovery, and Expression of Aequorea Green Fluorescent Protein, with a Note on an Unfinished Experiment*, volume 73, pages 785–796. Wiley, 2010. doi: 10.1002/jemt.20821.

J. Udensi, J. Loughman, E. Loskutova, and H. J. Byrne. Raman spectroscopy of carotenoid compounds for clinical applications-a review. *Molecules*, 27(24):32, 2022. doi: 10.3390/molecules27249017.

M. Van Riel, J. Kleinen Hammans, M. Van De Ven, W. Verwer, and Y. K. Levine. Fluorescence excitation profiles of β-carotene in solution and in lipid/water mixtures. *Biochemical and biophysical research communications*, 113:102–107, 1983. doi: 10.1016/0006-291X(83)90437-0.

H. Wu, J. V. Volponi, A. E. Oliver, A. N. Parikh, B. A. Simmons, and S. Singh. In vivo lipidomics using single-cell Raman spectroscopy. *Proceedings of the National Academy of Sciences of the United States of America*, 108(9):3809–3814, 2011. doi: 10.1073/pnas.1009043108.

Y. Yeeh. *Rhodotorula*, pages 1900–1905. Elsevier, Oxford, 1999. doi: 10.1006/rwfm.1999.1340.

L. Y. Zang, O. Sommerburg, and F. VanKuijk. Absorbance changes of carotenoids in different solvents. *Free Radical Biology and Medicine*, 23(7):1086–1089, 1997. doi: 10.1016/s0891-5849(97)00138-x.

M. Zia-Ul-Haq, S. Dewanjee, and M. Riaz. *Carotenoids: Structure and Function in the Human Body*. Springer, 2021. doi: 10.1007/978-3-030-46459-2.

# List of Figures

# List of Tables

# List of Abbreviations

| | |
|---|---|
| GAF | Green autofluorescence |
| GFP | Green fluorescence protein |
| VDE | Violaxanthin-de-epoxidase |
| ZE | Zeaxanthin epoxidase |
| ROS | Reactive oxygen species |
| FLIM | Fluorescence lifetime imaging |
| nd | Not detected |
| AcetAc | Acetic acid |
| TCM | Chloroform |
| EtOH | Ethanol |
| Min. oil | Mineral oil |
| THF | Tetrahydrofuran |
| RuBisCO | Ribulose-1,5-bisphosphate carboxylase/oxygenase |
| *H. pluvialis* | *Haematococcus pluvialis* |
| *R. glutinis* | *Rhodotorula glutinis* |